Proximity proteomics reveals a co-evolved LRRK2-regulatory network linked to centrosomes

Marita Eckert[1,4,5], Pasquale Miglionico[2,5], Francesca Izzi[1], Natalia De Oliveira Rosa[2], Benjamin Riebenbauer[1], Marius Ueffing[3], Francesco Raimondi[2*] and Christian Johannes Gloeckner[1,3*]

[1]German Center for Neurodegenerative Diseases, 72076 Tübingen, Germany;

[2]Laboratorio di Biologia Bio@SNS Scuola Normale Superiore, 56126 Pisa, Italy;

[3]Center for Ophthalmology, Institute for Ophthalmic Research, University of Tübingen, 72076 Tübingen, Germany

[4] Graduate School of Cellular and Molecular Neuroscience, University of Tübingen, 72074 Tübingen, Germany.

[5]contributed equally to this work.

Corresponding authors:

Christian Johannes Gloeckner (johannes.gloeckner@dzne.de)

Francesco Raimondi (francesco.raimondi@sns.it)

Abstract

Leucine-rich repeat kinase 2 (LRRK2) not only plays a vital role in familial forms of Parkinson's disease (PD) but also represents a risk factor for idiopathic PD. Its multi-domain architecture enables fine-tuned regulation of its biological function by orchestrating intra- and intermolecular interactions. Here, we present BioID proximity proteomes of LRRK2 that reveal new interactors, which we further characterize using a novel evolutionary and structural bioinformatics pipeline. Co-evolutionary analysis of the protein-protein interaction network identifies a structural and functional module enriched in cytoskeletal components associated with the centrosome and microtubules. In addition, structural modelling of binary interactions using AlphaFold-Multimer reveals distinct groups of interactors that engage LRRK2 in a manner dependent on specific conformations and epitopes. Furthermore, we identify distinct changes in the LRRK2 proximity proteome that are induced by the type I kinase inhibitor MLi-2 or by co-expression of the LRRK2 upstream effector RAB29. Depending on its activity state and conformation, these protein-protein interactions link LRRK2 to defined cellular sub-compartments, including centriolar satellites and vesicular sub-compartments.

Key words: LRRK2 interactome, proximity proteomics, BioID, Parkinson's disease, co-evolutionary analysis

Summary:

This study defines a comprehensive, LRRK2 interaction network by combining proximity proteomics with evolutionary and structural analyses, revealing how LRRK2 conformation and activity state dictate distinct protein-protein interactions. These findings link LRRK2 to conserved centrosomal, cytoskeletal, and vesicular pathways, providing mechanistic insight into its role in Parkinson's disease.

Key results:

- **Centrosome-linked LRRK2 network:** BioID combined with co-evolutionary analysis identifies a highly conserved module enriched in centrosomal and microtubule-associated proteins, including CYLD as a top co-evolved interactor.
- **Conformation-specific interactions:** AlphaFold-Multimer modelling reveals distinct classes of LRRK2 interactors that bind different domains and conformations ("locked" vs. "unlocked"), corresponding to specific cellular functions.

- **State-dependent rewiring of the interactome:** The type I inhibitor MLi-2 selectively redirects LRRK2 to centriolar satellite proteins, whereas RAB29 co-expression shifts LRRK2 interactions toward vesicular and lysosomal pathways.

Introduction

Parkinson's disease (PD) is the second most common neurodegenerative disease after Alzheimer's. It occurs mostly sporadically and is distributed with high frequency in the older generations. PD is characterized by a loss of dopaminergic neurons in the *substantia nigra* leading to the motor symptoms associated with the disease (Fahn, 2003). Several therapies targeting the symptoms, such as dopamine substitution, are used; however, no causative therapy currently exists. About 5–10% of PD cases are hereditary (Gasser *et al*, 2011). *LRRK2*, localized within the PARK8 locus and coding for the Leucine-rich repeat kinase 2, is one of the genes associated with familial forms of the disease but also represents a risk factor in idiopathic PD (Paisan-Ruiz *et al*, 2004; Simon-Sanchez *et al*, 2009; Zimprich *et al*, 2004). The multi-domain protein LRRK2 is an active protein kinase and, at least, mutations with confirmed disease segregation, including the most common G2019S variant within its kinase domain, augment its kinase activity (Kalogeropulou *et al*, 2022). This makes LRRK2 an important drug target (Kluss *et al*, 2022b). ATP-competitive LRRK2-specific kinase inhibitors for PD-treatment are under development and in clinical trials (Jennings *et al*, 2022). Nevertheless, structural changes of the lung observed in non-human primates indicate a relatively small therapeutic window and additionally challenge a long-term treatment with these compounds necessary to allow a life-long reduction of augmented LRRK2 pathway activation (Miller *et al*, 2023). For this reason, the identification of alternative drug targets within the LRRK2-associated pathways would be a potential solution for a better control of pathophysiological alterations associated with pathogenic forms of this protein, minimizing the risk of drug-induced lung pathologies. In addition, a larger group of patients beyond LRRK2 mutation carriers might benefit from targeting more common PD-associated pathways.

Various studies have demonstrated that LRRK2 functions in vesicle trafficking, including presynaptic vesicles as well as autophagy and lysosomal pathways (Piccoli *et al*, 2011; reviewed in: Follett & Farrer, 2021). In agreement with these cellular functions, LRRK2 phosphorylates a subset of Rab proteins, small G-proteins involved in vesicular transport, such as Rab8a and Rab10, which is elevated by PD-associated LRRK2 variants (Steger *et al*, 2017).

In common with other Roco proteins, LRRK2 features a remarkable complexity (Wauters *et al*, 2019). In fact, LRRK2 contains multiple scaffolding domains, not only involved in maintaining LRRK2 in an auto-inhibited state, as recently demonstrated by high-resolution structures of LRRK2 (Deniston *et al*, 2020; Myasnikov *et al*, 2021), but also in mediating protein–protein interactions, making LRRK2 a signaling hub possibly integrating multiple up- and down-stream signals (reviewed in: Manzoni *et al*, 2015). These studies suggest that the Roco protein LRRK2 is a tightly controlled protein kinase serving as hub and signal integrator and is most likely involved in context-specific, spatially

84 controlled cellular responses that appear evolutionarily conserved. Considerable effort has therefore
85 been spent on the investigation of the protein-protein interaction networks of LRRK2, mainly using
86 affinity-based methods. Various studies have investigated the LRRK2 interactome across different
87 cellular contexts and model organisms (Islam et al, 2016; Meixner et al, 2011; Piccoli et al, 2011;
88 Piccoli et al, 2014). These data have been curated in public databases such as IntAct or STRING and
89 subjected to meta-analysis to dissect functional LRRK2 signaling networks (Gloeckner & Porras,
90 2020; Manzoni *et al*, 2015; Zhao *et al*, 2024; Zhao *et al*, 2023). However, most approaches rely on
91 immunoprecipitation or pull-down methods, which are biased toward stable complexes and may
92 underrepresent transient interactions.
93 To overcome these limitations, we applied the BioID proximity labeling approach to identify LRRK2
94 interaction partners in living cells. Using BioID with three different tags, we define the proximity
95 proteome of LRRK2 under basal conditions. In addition, using a newly designed bioinformatics
96 workflow that estimates co-evolution of interacting partners based on their co-occurrence across
97 sequenced genomes, we show that the resulting BioID datasets are enriched for interactions with
98 high co-evolution scores, comparable to confirmed direct interactions. This approach identifies a
99 cluster of interactors with strong co-evolution to LRRK2, enriched in cytoskeletal proteins associated
100 with centrosomal and ciliary dynamics. Furthermore, structural modeling of binary complexes using
101 AlphaFold-Multimer reveals distinct conformations and interaction interfaces linked to specific
102 functional processes. Finally, to further stratify the LRRK2 interactome, we analyzed experimentally
103 defined conformational states, including co-expression with the upstream effector RAB29 and
104 stabilization of an active-like kinase conformation by a type I inhibitor (Taylor et al, 2020; Wauters et
105 al, 2019). Notably, MLi-2, but not GZD-824, enriched a specific sub-interactome associated with
106 centriolar satellites.
107

108 **Results**

109 *Definition of cellular LRRK2 proximity proteomes with BioID1, BioID2 and miniTurbo.*

110 To characterize the LRRK2 interactome, we applied the proximity labeling approach BioID, which
111 enables the identification of protein–protein interactions in living cells, including transient
112 interactions. To define the LRRK2 proximity proteome, we generated N-terminal fusion constructs
113 using the original BioID (BioID1), BioID2, and miniTurbo tags.
114 All constructs were functionally validated to confirm biotinylation activity and to ensure that the tags
115 did not interfere with LRRK2 function. Western blot analysis demonstrated efficient biotinylation for
116 all constructs (Appendix Figure S1), with BioID2 and miniTurbo showing higher labeling efficiency

117 compared to BioID1. We further confirmed that the fusion proteins retained kinase activity by
118 assessing phosphorylation of the physiological LRRK2 substrate Rab10 at Thr73 (Appendix Figure S1).
119 Following validation, all three constructs were used to determine their interactomes upon transient
120 expression in HEK293T cells. To increase stringency, a tag-only control was used as reference. For
121 relative comparisons, expression levels were adjusted in preliminary experiments and consistently
122 verified by Western blot analysis of cell lysates. The use of a tag-only control enabled efficient
123 exclusion of endogenously biotinylated proteins, whose labeling is inherently increased by biotin
124 supplementation.
125 Data from all three proximity proteomes were analyzed using SAINTexpress and, independently, by
126 label-free quantification (LFQ) combined with an FDR-controlled t-test implemented in Perseus
127 (Tyanova et al, 2016). To further refine the dataset, we applied a bioinformatics pipeline
128 incorporating co-evolution analysis of interacting proteins and structural modeling using AlphaFold-
129 Multimer (Figure 1A).
130 Using LFQ, 168, 312, and 241 proteins were identified as significantly enriched in the LRRK2
131 condition compared to the tag-only control for BioID1, BioID2, and miniTurbo, respectively (Figure
132 1B; Dataset EV1). SAINTexpress (Teo et al, 2014), followed by filtering against the CRAPome
133 database (Mellacheruvu et al, 2013), provided a more stringent set compared to LFQ-based analysis.
134 Based on this approach, we defined a non-redundant set of 208 unique interactors, hereafter
135 referred to as the "BioID set," which was subjected to downstream bioinformatics analysis.

136 *Functional-enrichment analysis of the LRRK2 proximity proteome*

137 We compared the LRRK2 BioID interactome with a reference LRRK2 interactome available from
138 IntAct (Orchard *et al*, 2014). We found that only 54 interactors in the filtered BioID set were
139 previously reported to be associated with LRRK2, whereas the majority (154) have not been
140 reported before (Figure 2A, B). By integrating the LRRK2 BioID interactome with known interactions
141 from IntAct, we defined modules of proteins that interact not only with LRRK2 but also with each
142 other, thereby revealing structured interaction networks (Figure 2A). Among the enriched
143 intracellular and cytosolic compartments, we found terms related to microtubules (e.g. Microtubule
144 Cytoskeleton, FDR = 5.83E-15) and Centrosome (FDR = 1.43E-13), emphasizing the importance of
145 LRRK2 in microtubule organization (Figure 2C), and representing the largest module of interacting
146 proteins in the network (Figure 2A). In addition, we also found processes related to cell cycle and
147 mitosis (e.g. "Regulation of mitotic cell cycle", FDR = 9.71E-08) (Figure 2D).
148 Multiple protein domains instances are significantly enriched within the list of identified LRRK2
149 interaction partners (Figure 2E). In particular, we found that the Armadillo-type fold instance is the
150 most enriched one (FDR = 9.58E-06), which is found in 21 distinct interactors, followed by other

151 domains with lower, but still significant, degree of enrichment, such as "Forkhead-associated (FHA)
152 domain" (Almawi *et al*, 2017), found in six distinct proteins, the "DIX domain" (Ehebauer & Arias,
153 2009; Kafka *et al*, 2014) found in four proteins, the "K Homology domain, type 1" (Grishin, 2001)
154 found in six proteins and "Ubiquitin-like domain superfamily" (FDR < 0.05), the latter being found in
155 11 distinct interacting proteins. Interestingly, LRRK2 and its Drosophila orthologue dLRRK have been
156 demonstrated to functionally interact with the Forkhead box transcription factor FoxO1/dFoxO. In
157 particular, LRRK2-mediated phosphorylation of FoxO1 enhances its transcriptional activity leading to
158 neuronal toxicity (Kanao *et al*, 2010).

159 *A cluster of proteins involved in centrosome/ microtubular dynamics are most co-evolved with LRRK2*

160 We analyzed the extent of co-evolution of LRRK2 with its interactors to prioritize the most conserved
161 relationships associated to LRRK2's functions. We derived a metric for the co-evolution between two
162 interacting proteins based on the degree of co-presence, assessed through a Jaccard score, of
163 interacting gene pairs in sequenced genomes available from a reference orthology database (e.g.
164 OMA, see Methods). We found that such simple co-evolutionary metric is informative about non-
165 enzymatic, direct interactions as well as stable complexes at a human interactome-wide level
166 (Meldal *et al*, 2022; Miglionico *et al*, 2024; Orchard *et al*, 2014) (Dataset EV2A). We found similar
167 trends when focusing on LRRK2 interactions reported in IntAct, with "non-enzymatic direct" PPIs
168 being characterized by a significantly higher Jaccard score compared to those categorized as
169 "association" or "physical interaction" (Figure 3A). Intriguingly, we found that the distribution of co-
170 evolution metrics calculated for BioID interactors is significantly higher than most IntAct categories
171 (i.e. "association", "physical", "enzymatic direct") and it is as high as the non-enzymatic direct
172 interactions (Figure 3A). This result suggests that interactors captured within the BioID dataset may
173 represent stable, direct interaction partners of LRRK2 with whom they co-evolved. Likewise, simple
174 co-evolution scores are predictive for LRRK2 direct interactions, particularly the non-enzymatic
175 direct ones (Figure 3B; ROC AUC = 0.715). In the case of the LRRK2 interactome, we found that this
176 co-evolutionary metric is more predictive of non-enzymatic direct interaction compared to another
177 co-evolution estimate, i.e. Mutual Information (ROC AUC = 0.66; Appendix Figure S2), which is
178 instead more predictive at a human proteome scale (Miglionico *et al*, 2024).
179 We used the co-evolution metric to cluster LRRK2 and its interactors, which revealed groups of
180 proteins characterized by reciprocal high co-evolution (Figure 3C). The different groups of
181 interactors are also characterized by specific biological processes, which are overall mutually
182 exclusive to each other, suggesting that clusters of co-evolved proteins underpin specific functional
183 interactions and biological processes (Appendix Figure S3). Notably, the cluster containing LRRK2
184 (i.e. Cluster 2) is characterized by on average higher co-evolution and several highly co-evolved

185 proteins (Figure 3C). The top 10 proteins of Cluster 2 showing highest co-evolution are summarized
186 in Table 1. By mapping members of this cluster onto the STRING functional interaction network
187 (Figure 3D, see Methods), we found functional interactions for most of the members, including
188 LRRK2. Overall, STRING yielded a highly significant PPI enrichment (P = 1.0E-16), suggesting that
189 these proteins are more likely to interact with themselves than with randomly selected proteins.
190 Moreover, network topology analysis delineated two distinct submodules: the first encompassing
191 LRRK2 together with proteins predominantly linked to Wnt signaling (FDR = 0.0013; Figure 3E), and
192 the second consisting of proteins implicated in cytoskeletal processes ("Protein localization to
193 microtubule cytoskeleton"; FDR = 2.18E-05), centrosome dynamics ("Loss of Nlp from mitotic
194 centrosomes"; FDR = 0.00086) and centriole organization ("Centriole"; FDR = 1.11E-05). Consistently,
195 Cluster 2 displayed strong enrichment for cellular component terms, most notably "Microtubule
196 Cytoskeleton" (FDR = 2.10E-12) and "Centrosome" (FDR = 1.01E-12) (Dataset EV2B). Interestingly,
197 CYLD is the most co-evolved protein of LRRK2, a deubiquitinase that acts as a negative regulator of
198 dopamine neuron survival in Parkinson's disease (Pirooznia et al., 2022), but has not yet been
199 reported to directly interact with LRRK2. Notably, CYLD emerges as a critical bridging element that
200 connects the two principal submodules within Cluster 2's interactome (Figure 3D).
201 On the other hand, Cluster 1 is characterized by distinct processes, such as FAR/SIN/STRIPAK
202 complex (P = 0.0012; Dataset EV2 B). Taken together, these results suggest that our co-evolution-
203 based approach was able to identify a group of LRRK2 interacting proteins, mostly associated to
204 microtubule and centrosome functions via the formation of stable, supramolecular complexes.
205 Likewise, co-evolution-based clustering of LRRK2 interactors from IntAct shows interactors such as
206 RAB29, RAB12, LRRK1 or SNCA among the most co-evolved partners that cluster with LRRK2
207 (Appendix Figure S4), confirming the tight evolutionary constraint on LRRK2's functional regulation.

208 After validating CYLD as part of the LRRK2 proximity proteome by Western blot analysis (Figure 3F),
209 we investigated the functional relevance of this association by assessing whether CYLD influences
210 LRRK2 abundance. To this end, LRRK2 wild-type or the pathogenic Y1699C variant was co-expressed
211 with CYLD or an empty vector control. Y1699C was chosen, as this variant shows a robust increase in
212 Rab phosphorylation (Kalogeropulou *et al*, 2022) and reduced steady-state protein levels under our
213 experimental conditions. As classical ECL-based Western blot did not allow reliable quantification of
214 the large protein LRRK2 (286 kDa), we used a capillary-based Western system with fluorescent
215 detection.
216 CYLD co-expression was associated with increased steady-state LRRK2 levels across two independent
217 experiments (N = 6 biological replicates each), with the effect being more pronounced for the

218 Y1699C variant. Wild-type LRRK2 showed a smaller increase, consistent with a weaker trend (Figure
219 3G; Appendix Figure S5A).
220 Because CYLD preferentially acts on K63-linked chains, we repeated the experiment with additional
221 co-expression of either wild-type ubiquitin or a K63-only ubiquitin mutant, which restricts linkage to
222 lysine 63 (Lim *et al*, 2005). However, while replicating the effects seen without Ubiquitin
223 overexpression, these data do not allow conclusions about the contribution of specific ubiquitin
224 linkage types (Appendix Figure S5B).

225 *AF-based modelling reveals a discrete repertoire of conformations and interfaces shaping the LRRK2*
226 *interactome*

227 We predicted 3D complexes for binary interactions of LRRK2 and 196 partners in the BioID dataset
228 via AlphaFold-multimer (AF) and characterized their interfaces and conformations (Figure 4A).
229 We structurally aligned LRRK2 conformations in the different complexes by superimposing the
230 monomeric LRRK2 chains and then calculating the pairwise Root Mean Squared Deviation (RMSD) of
231 all the possible pairs (Figure 4A; Methods). We performed hierarchical clustering of LRRK2 structures
232 based on RMSD, through which we identified two main clusters (Figure 4B). A smaller one is
233 characterized by conformations with lower deviation from the inactive LRRK2 structure (PDB ID:
234 7LHW), which we termed "locked" (Figure 4B-D). The main structural hallmarks characterizing the
235 "locked" conformation, which are inherited by the experimental inactive LRRK2 structure
236 (PDB:7LHW) (Myasnikov *et al*, 2021), are the LRR wrapping around the catalytic domains, particularly
237 the kinase, and a contact formed by the extended loop within the LRR repeats, which includes the
238 hinge helix, and the C-terminal WD40 (Myasnikov *et al*, 2021). A larger cluster comprised
239 conformations characterized by a greater deviation from the inactive structure due to major
240 rearrangements of the LRR, ROC and COR domains, which we termed "unlocked" (Figure 4B-D). Such
241 conformations are reminiscent of the ones that we observed in the predicted LRRK2-RAB10 complex,
242 which we validated as the AF-predicted conformation best accommodating experimental XL-MS data
243 (preprint: Guaitoli *et al*, 2023). Intriguingly, we found that proteins interacting with LRRK2 in these
244 two alternative conformations are associated with distinct evolutionary and functional properties.
245 Indeed, LRRK2's complexes in the "locked" conformations are characterized by a significantly lower
246 RMSD (P = 3.81E-20; Figure 4D) and higher co-evolution (P = 1.33E-3; Figure 4E) than the complexes
247 in the "unlocked" conformations. The two groups are also characterized by largely exclusively
248 enriched processes (Figure 4F). In particular, the interactors engaging with LRRK2 in the locked
249 conformation are significantly associated with processes linked to centriolar satellites (P = 4.76E-10)
250 and cilium assembly (P = 0.0001) (Figure 4G; Dataset EV2C). Those interacting with the unlocked
251 conformations are associated with a higher number of enriched processes, including cluster-specific

252 ones such as cytoskeleton (P = 4.53E-09) or the microtubule organizing center MTOC (P = 6.40E-07).
253 Hence, the predicted LRRK2 conformational switch might be relevant in orchestrating the interaction
254 with partners associated with distinct functions.
255 We also explored patterns of engagement of interactors with the different regions of the LRRK2
256 multi-domain architecture. To this end, we considered the distribution of distance probabilities (i.e.
257 distograms) generated by AF for each binary interaction and mapped the most likely interacting
258 residues of the partners with respect to LRRK2 positions. We used these partner-specific interaction
259 fingerprints to cluster the interactome and identified four major groups of proteins, each named
260 according to the LRRK2 3D interface involved in the interaction (Figure 5A; Dataset EV2 D; see
261 Methods). The Core cluster comprises partners that interact with the LRR–ROC–COR–KIN domains
262 and was named accordingly, as these domains represent the most evolutionarily conserved regions
263 of LRRK2 (Figure 5A, B). The WD40 cluster includes complexes involving the homonymous domain
264 (Figure 5A, C), while the ARM cluster comprises proteins engaging a newly identified site within the
265 Armadillo domain (Figure 5A, D). Lastly, the "Other" cluster contains proteins with alternative
266 interaction modalities or no clearly defined binding interface (Figure 5A). Complexes predicted to
267 interact with the Core group displayed significantly higher AlphaFold confidence scores compared to
268 those interacting with the WD40 domain (P = 1.14E-8) or via "Other" interaction modalities (P =
269 4.86E-14; Figure 5E). Complexes of the Core group show a significantly higher RMSD of the LRRK2
270 chain compared to the WD40 group (P = 4.05E-3; Figure 5F), whose interactors bind LRRK2 in both
271 locked and unlocked conformations (see below). In the Core cluster we found established LRRK2
272 interactors, such as DVL1-2, confirming the known interaction mechanism through the ROC-COR
273 domains (Sancho *et al*, 2009). In the same cluster, we also found novel interactors discovered within
274 the BioID set, such as e.g. CYLD interacting through the Core interface in a similar way. A second
275 cluster (WD40) displayed higher likelihood of interaction with the WD40 domain (Figure 5A, C), with
276 predicted complexes characterized by a similar interface involving the binding of a short, disordered
277 peptide stretch to a conserved crevice formed by β-propeller loops of the WD40 domain (Figure 5C).
278 WD40 domain binders might bind to LRRK2 in either locked or unlocked conformation (Figure 5A, F),
279 as also suggested by a bi-modal distribution of the LRRK2 chain RMSD (Figure 5F). These interactors
280 also displayed significantly higher co-evolution with respect to "Other" LRRK2 interactors (P = 5.57E-
281 4; Figure 5G). The ARM cluster involves proteins showing binding preferences for a new docking site
282 on the Armadillo domain, centered around residues 500-600 and mediating the interaction with
283 proteins such as AXIN1 (Figure 5A, D). The larger cluster (Other) contains proteins interacting with
284 weaker likelihood and variable docking sites (Figure 5A). Among these, we also found proteins
285 engaging with two additional ARM docking sites, including one (around aa 240) which has been

286 recently shown to interact with RAB12 (Dhekne *et al*, 2023; Li *et al*, 2024) and mediate a RAB29-
287 independent LRRK2 Kinase activity activation (Purlyte *et al*, 2018; Zhu *et al*, 2023), which is predicted
288 to interact with proteins such as KIF16B. A third ARM binding region, encompassing aa 354-444,
289 corresponds to the RAB29 interaction interface found in the recently determined RAB29-bound,
290 tetrameric LRRK2 structure (Zhu *et al*, 2023), and it is the predicted interface for proteins such as
291 NBR1 and MON2.

292 Overall, these results further support the hypothesis that interactors *de-novo* identified by proximity
293 labelling may physically interact with LRRK2 domains through specific conformations and contact
294 interfaces. Interactors lacking a strong interaction probability in the distogram might represent
295 proteins interacting with LRRK2 either transiently or indirectly.

296 *Type I but not type II inhibitors lead to conformational changes directing LRRK2 to centriolar satellites*

297 As mentioned above, LRRK2 adopts multiple conformations through which it engages with its
298 interactors. Effector-mediated oligomerization to an asymmetric tetramer has been demonstrated
299 to switch LRRK2 to an active conformation (Zhu *et al*, 2023). In addition, ATP-competitive kinase
300 inhibitors can stabilize different conformations. While type I inhibitors stabilize the kinase domain in
301 an active-like conformation, type II inhibitors stabilize the inactive conformation of the kinase
302 domain (Deniston *et al*, 2020; Raig *et al*, 2025; Zhu *et al*, 2024). Interestingly, type I but not type II
303 inhibitors lead to a rapid dephosphorylation of LRRK2 phospho-sites in an interdomain space
304 downstream of the hinge-helix which locks LRRK2 in a compact inactive fold by binding the C-
305 terminal WD40 domain (Kalogeropulou *et al*, 2022; Myasnikov *et al*, 2021). We hypothesized that
306 specific inhibitors could distinguish the proximity proteome of LRRK2 in its active versus inactive
307 conformation. To test this, we compared the LRRK2 proximity proteome in HEK293 cells stably
308 expressing miniTurbo-tagged LRRK2 following treatment with the type I kinase inhibitor MLi-2, the
309 type II inhibitor GZD-824 (previously shown to inhibit LRRK2 in cells (Kalogeropulou *et al*, 2022;
310 Tasegian *et al*, 2021)), or a DMSO control. Western blot analysis of LRRK2 pS935 and pT73-Rab10
311 confirmed effective inhibition under these conditions (Appendix Figure S6A). Quantitative label-free
312 analysis combined with an FDR-controlled t-test revealed that only MLi-2 treatment led to the
313 enrichment of a distinct set of proteins associated with cilia assembly and centriolar satellites in the
314 LRRK2 proximity proteome (Figure 6A–E, Appendix Figure S6B), a pattern not observed with GZD-
315 824. Intriguingly, interactors determined in the presence of the MLi-2 inhibitor are characterized by
316 a significantly higher co-evolution (Figure 6F) compared to other BioID interactors. The complete list
317 of significantly enriched proteins (MLi-2 vs. DMSO) is shown in Table 2. Additional information is
318 provided in Dataset EV1.

319 To functionally validate the interaction between LRRK2 and centriolar satellites, we first confirmed
320 that LRRK2 associates with key components of these membrane-less organelles, including the
321 central scaffold protein PCM1 and the centrosome maturation factor SSX2IP (Barenz *et al*, 2013).
322 Both proteins were enriched in LRRK2 proximity proteomes following biotin treatment, with their
323 interaction further enhanced by the LRRK2 inhibitor MLi-2. To further substantiate LRRK2's
324 association with centriolar satellites, we employed RNA interference to deplete PCM1, a strategy
325 known to disrupt satellite integrity (Dammermann & Merdes, 2002). As expected, PCM1 depletion
326 led to its absence from the LRRK2 proximity proteome and also abolished the association between
327 LRRK2 and SSX2IP. Remarkably, SSX2IP was entirely absent from LRRK2 proteomes regardless of MLi-
328 2 treatment, indicating that LRRK2's interaction with SSX2IP is dependent on intact centriolar
329 satellites. Finally, we asked whether the MLi-2–induced dephosphorylation of serine 935—located
330 near the LRRK2 hinge helix—is affected by satellite disruption. However, PCM1 knock-down did not
331 influence serine 935 dephosphorylation, suggesting that this post-translational modification occurs
332 independently of centriolar satellite integrity (Figure 6D, Appendix Figure S6C).

333 *RAB29 co-expression directs LRRK2 to well established lysosomal protein networks*

334 It has been previously shown that LRRK2 interacts with the RAB29/RAB32/RAB38 family of small G-
335 proteins and subsequently locates to post-Golgi endomembranes (Beilina *et al*, 2014; McGrath *et al*,
336 2021; Vides *et al*, 2022; Waschbusch *et al*, 2014). Furthermore, RAB29 not only recruits LRRK2 to
337 lysosomal membranes but also induces its tetramerization (Zhu *et al*, 2023). For this reason, we
338 performed the BioID experiment following RAB29 co-expression to determine PPI networks
339 associated with the activated oligomeric state of LRRK2. In addition to mT-LRRK2, either RAB29 or an
340 empty vector were co-expressed. The resulting differential proximity proteome showed differentially
341 enriched proteins only for the condition where RAB29 was co-expressed, demonstrating that a small
342 portion of LRRK2 was recruited by RAB29 with lesser impact on the total proximity proteome (Figure
343 6G). While we did not observe any significant difference in terms of co-evolution of the RAB29
344 differential proteome with respect to the BioID one (Figure 6F), we found significant enrichment in
345 proteins involved in vesicular transport, including the post-Golgi/ lysosomal compartment as
346 revealed by an LFQ analysis combined with an FDR-controlled T-test (Figure 6H, I). In particular,
347 known LRRK2 effectors, namely RAB8A (Steger *et al*, 2017) and SPAG9 (Boecker & Holzbaur, 2021;
348 Bonet-Ponce *et al*, 2020; Kluss *et al*, 2022a) were among the enriched proteins (Figure 6G, H). Also,
349 VAMP7, which is part of a SNARE complex mediating autophagosome-lysosome fusion (Jian *et al*,
350 2024), was among the significantly enriched proteins (Figure 6G, H). VAMP7-LRRK2 physical

351 interaction has recently been described (Filippini *et al*, 2023). The complete list of significantly
352 enriched proteins is shown in Table 3. Additional information is provided in Dataset EV1.

353

354 *MLi-2 and RAB29 differently modulate the shape of the LRRK2 interactome*

355 We constructed 3D models of binary complexes between LRRK2 and its partners from the MLi-2–
356 and RAB29-dependent interactomes, and examined both the complex interfaces and the
357 conformational states of LRRK2 (Vides *et al*, 2022).
358 Interface-based clustering suggests that MLi-2–dependent interactors engage with LRRK2 through
359 specific domain regions, particularly the ones involving terminal domains (Figure EV1 A), while they
360 are predicted to engage little with the catalytic domains, particularly the kinase, which is consistent
361 with the MLi-2 inhibitor function. In the RAB29-dependent LRRK2 interactome, we see instead a
362 more variable pattern of engaged interfaces. In particular, predictions for this interactome revealed
363 a cluster of proteins interacting with LRRK2 through the ROC-COR-KIN domains, including the RAB8A
364 substrate (Figure EV1B), suggesting that in the context of RAB29 overexpression several partners
365 might bind in a substrate-like manner. Notably, this interaction modality is absent in the predicted
366 binary complexes of the MLi-2–bound interactome, confirming that the inhibitor prevents LRRK2
367 from binding substrate-like partners. Moreover, we further validated the capability of the distogram-
368 based interface-fingerprint to discriminate functionally relevant LRRK2 interactors. We predicted 3D
369 complexes between LRRK2 and known interacting Rabs and found that Rab substrates clustered
370 separately from other interacting Rabs with distinct functions, such as RAB29 and RAB32 (Figure
371 EV1B).
372 From a conformational perspective, we pooled the RAB29- and MLi-2–dependent interactomes and
373 clustered LRRK2 structures based on RMSD, which likewise revealed distinct locked and unlocked
374 clusters (Figure 7A). Interestingly, Rab8a acting downstream of LRRK2 and Rab29 acting upstream of
375 LRRK2 engage with LRRK2 in two different conformations: While Rab8a engages with the unlocked
376 state (Figure 7B), structural modelling suggests that Rab29 engages with the locked state (Figure 7C).
377 Interactors from the RAB29-dependent interactome are predicted to bind LRRK2 in both
378 conformations, with a particular enrichment in the unlocked state. Conversely, MLi-2–dependent
379 interactors were significantly enriched in the locked LRRK2 conformation (Fisher's exact test, P =
380 0.023), further suggesting that the inhibitor-bound state favors engagement with partners that,
381 unlike substrates, do not require interaction with the kinase domain (Figure 7A). Also for these
382 interactors, the locked conformation has a significantly lower RMSD (P = 3.85E-6; Figure 7D) and a
383 tendency towards higher co-evolution (Figure 7E). Notably, enrichment analysis of interaction

384 partners grouped by conformational cluster revealed even stronger cluster-specific associations,
385 with only a single process shared between partners in the locked and unlocked conformations
386 (Figure 7F, G; Dataset EV2E).

387

388 **Discussion**

389 The systematic analysis of the interactomes of disease-associated proteins is a powerful tool to
390 dissect molecular networks and to identify pathways relevant for the molecular pathophysiology, for
391 example demonstrated by the comprehensive interactomic network underlying the assembly and
392 homeostasis of primary cilia (Boldt *et al*, 2016). Given its complex domain structure and tight
393 regulation, LRRK2 is most likely representing a scaffold protein orchestrating distinct signaling
394 complexes, which makes the analysis of its PPI networks an attractive approach to dissect context-
395 specific signaling pathways (Gloeckner & Porras, 2020). While a wealth of data is available for
396 affinity-based identification of protein-protein interactions, which are biased toward stable
397 complexes, there is an unmet need for the dissection of less stable and transient PPIs. The rapid
398 development of biotin-based proximity labelling technologies has made it possible to explore
399 previously inaccessible regions of the interactome (Qin *et al*, 2021). Consequently, APEX and BioID
400 have emerged as widely used techniques for dissecting protein-protein interaction (PPI) networks (Li
401 *et al*, 2017). For LRRK2, the first APEX2 dataset only recently became available (Bonet-Ponce *et al*,
402 2020). In the present study, we systematically investigated the proximity interactome of LRRK2 using
403 three different BioID tags—BioID1, BioID2 and miniTurbo. The resulting data showed the expected
404 overlap with previously reported interactors, while also uncovering numerous novel candidates.
405 However, several anticipated interactors, including Rab proteins, were not detected in the initial
406 BioID experiments. Nevertheless, Rab8a was identified together with Rab29 upon co-expression of
407 Rab29, which may reflect conformational constraints that reduce accessibility for BioID-mediated
408 biotinylation. Consistent with these observations, a recent comparison of BioID and co-
409 immunoprecipitation in the context of the nuclear pore complex demonstrated that the two
410 approaches provide functionally relevant yet complementary interaction profiles (Moreira *et al*,
411 2023).

412 To identify direct LRRK2 interactors with high confidence from the proximity proteomes, we applied
413 a newly developed bioinformatic pipeline relying on co-evolution, co-expression and protein domain
414 architecture to predict interaction type (preprint: Miglionico *et al*, 2024). This pipeline allowed the
415 identification of a group of proteins within the proximity proteome showing a high degree of co-
416 evolution with LRRK2 which is highly enriched in proteins associated with the centrosome. This is

417 particularly interesting as pathogenic LRRK2 has previously been shown to lead to a centrosome
418 cohesion defect as well as to a shortening of primary cilia (Dhekne *et al*, 2018; Khan *et al*, 2024; Lara
419 Ordonez *et al*, 2022). Furthermore, defects in primary cilia emerge as a new pathophysiological
420 scheme connecting different genes involved in mendelian forms of Parkinson's disease (Mohd Rafiq
421 *et al*, 2024; Schmidt *et al*, 2022). Strikingly, within the cluster of proteins showing the highest co-
422 evolution with LRRK2 (Cluster 2), the top-ranked interactor was the deubiquitinase CYLD, a key
423 effector in primary cilia biology. Preliminary data further indicate that CYLD co-expression increases
424 the levels of the pathogenic LRRK2 Y1699C variant, which exhibits lower steady-state protein levels
425 than wild-type LRRK2. In fact, this DUB has been shown to control apical docking of basal bodies in
426 ciliated epithelial cells (Eguether *et al*, 2014). It also regulates centrosomal satellites proteostasis by
427 counteracting the E3 ubiquitin ligase MIB1 (Douanne *et al*, 2019). CYLD has also been shown to
428 deubiquitinate Cep70 and to inactivate HDAC6 thereby mediating ciliogenesis (Yang *et al*, 2014).
429 Interestingly, a missense mutation has recently been shown to be a causative gene for FTD-ALS
430 (Dobson-Stone *et al*, 2020). Most importantly, as the deubiquitinase CYLD is part of the PINK1/Parkin
431 pathway to regulate cellular levels of PARIS (ZNF746), it is a critical regulator of mitochondrial
432 biogenesis thereby acting as a negative regulator of dopamine neuron survival in Parkinson's
433 disease. In fact, CYLD inhibition has been shown to ameliorate mitochondrial pathologies in cellular
434 PD models which makes CYLD a promising target for therapeutic intervention for PD and other
435 neurodegenerative diseases (Pirooznia *et al*, 2022). The E3 ligase Parkin preserves mitochondrial
436 homeostasis via the PARIS/PGC-1a axis (Stevens *et al*, 2015; Zheng *et al*, 2017). Noteworthy, the PD
437 risk variant LRRK2 G2385R has recently been shown to alter mitochondrial biogenesis via the PGC-1a
438 pathway, leading to reduced PGC-1a levels similarly to a Parkin knock-out in DA neurons (Kumar *et*
439 *al*, 2020; Xue *et al*, 2023). Parkin-deficient DA neurons show increased PARIS and decreased PGC-1a
440 levels (Kumar *et al*, 2020). In conclusion, this indicates that LRRK2/CYLD signaling, at one hand, and
441 Parkin signaling at the other, might converge on PARIS.

442 The second most co-evolved interactor found in Cluster 2 was the cilia-associated protein CEP85,
443 which plays a role in centrosome disjunction (Chen *et al*, 2019). This is of particular interest as
444 pathogenic LRRK2 variants lead to a centrosomal cohesion phenotype in patient-derived cells (Lara
445 Ordonez *et al*, 2019). Notably, the cohesion phenotype is also seen in EBV-transformed
446 lymphoblastoid cell lines from iPD patients which can be reverted by LRRK2 kinase inhibition
447 (Naaldijk *et al*, 2024). Importantly, Cluster 2 also contains the autophagy cargo protein
448 p62/sequestosome-1. This protein has previously been identified as LRRK2 interactor and substrate
449 (Kalogeropulou *et al*, 2018; Park *et al*, 2016). SQSTM1 is also linked to PD pathophysiology via the
450 Pink1/Parkin pathway (Shin *et al*, 2020). In addition, Cluster 2 points towards other pathways which

451 have been previously linked to PD pathology. In particular, SNAP47 is part of the STX17-SNAP47-
452 VAMP7/8 pathway, which has been shown to be involved in selective autophagy – a process not only
453 essential for the homeostasis of primary cilia but also for mitophagy (Jian *et al*, 2024). Phospho-
454 ubiquitin chains generated by PINK1/Parkin activity can recruit autophagy adaptors including the
455 ubiquitin adaptor SQSTM1/p62 linking the PINK1/Parkin-dependent pathway to mitophagy (Geisler
456 *et al*, 2010). All three proteins participate in the recruitment of the autophagy machinery to aged or
457 dysfunctional mitochondria, which are eventually enclosed inside an autophagosome and subjected
458 to the lysosome for degradation (Wilhelm *et al*, 2022).

459 Interestingly, also the kinesin motor protein and PX-domain containing protein KIF16B was among
460 the top hits which is involved in vesicle trafficking and receptor recycling. It binds to PdIns(3)P by its
461 unique PX domain and promotes the circulating cargo movement from early endosomes to the
462 plasma membrane (Li *et al*, 2020). Interestingly, it has been found to be associated with lipid
463 droplets (Bersuker *et al*, 2018). In turn, increased RAB8a phosphorylation by pathogenic LRRK2
464 variants, has been shown to promote lipid storage (Yu *et al*, 2018), indicating that the functional
465 interaction of LRRK2 and KIF16B might contribute to alterations in the neuronal lipid homeostasis
466 associated with PD pathology (Hallett *et al*, 2019).

467 Furthermore, conformational changes induced by MLi-2 binding—leading to rapid and nearly
468 complete dephosphorylation of LRRK2 within a disordered domain downstream of the hinge helix—
469 position LRRK2 in proximity to a molecular network centered around PCM1, OFD1, and CEP131,
470 strongly supporting a link between LRRK2 and centriolar satellites. Strikingly, the proteins interacting
471 with LRRK2 in the presence of MLi-2 displayed the highest degree of co-evolution, suggesting that
472 the connection between LRRK2 and centriolar satellites is highly conserved. The conformational
473 changes induced by binding of type I inhibitors might result in a phase transition of LRRK2 into
474 centriolar satellites preventing 14-3-3 binding and thereby shifting the equilibrium towards the
475 dephosphorylated protein. A similar mechanism has been shown for CEP131, which is extracted
476 from centriolar satellites by phosphorylation and subsequent binding of 14-3-3 (Tollenaere *et al*,
477 2015). Centriolar satellites not only play an essential role in the biogenesis of primary cilia (Hall *et al*,
478 2023) but also play a role in the degradation of proteins by driving the assembly of aggresomes
479 (Prosser *et al*, 2022). In fact, also LRRK2 has been shown to interfere with aggresome formation
480 preceding autophagic clearance (Bang *et al*, 2016). Nevertheless, one caveat might be seen in the
481 fact that LRRK2 inhibition with type I inhibitors induces its destabilization and degradation
482 (Lobbestael *et al*, 2016).

483 Structural prediction of LRRK2 binary complexes with AF revealed distinct interfaces within each
484 determined interactome. While several interactors preferentially engage with the catalytic core of
485 the protein, including the ROC and KIN domains, others are more likely to interact on terminal
486 domains (e.g. ARM or WD40). We predicted the interaction on the kinase domain for several
487 interactors of the BioID interactome as well as the one obtained in the presence of RAB29 over-
488 expression, including the known substrate RAB8A. The engagement in a substrate-like fashion with
489 the catalytic core entails the opening of the LRRK2 structure, with the detachment of the LRR and
490 rearrangement of the entire N-term domains. We previously showed that this conformation, that we
491 similarly predicted for the LRRK2:RAB10 complex, is compatible with distance restraints obtained by
492 mass spectrometric mapping of chemical crosslinking sites via XL-MS (Guaitoli *et al*, 2023).
493 Moreover, when superimposed onto the active-like conformation of the most recent LRRK2
494 tetrameric structure, these predicted complexes fit well within the oligomer, without steric clashes
495 between the modeled LRRK2 chain and the rest of the tetramer, further supporting their structural
496 plausibility (Guaitoli et al, 2023). We speculate that partners engaging in this manner may represent
497 putative substrates or function as regulators of kinase domain activity. Strikingly, such interaction
498 interfaces were rarely observed for interactors enriched in the presence of the MLi-2 inhibitor,
499 which preferentially bind the locked conformation of LRRK2.

500 In conclusion, combining proximity proteomics with co-evolutionary and structural information
501 helped identify distinct molecular networks linking LRRK2 to centrosomal biology and primary cilia.
502 The data may foster future functional analysis to further dissect these pathways to get a detailed
503 picture of the molecular pathophysiology underlying the cilia phenotypes caused by genetic variants
504 in different genes underlying familial forms of Parkinson's disease.

505

506 **Methods**

507 ***Cloning and generation of the stable miniTurbo-LRRK2 cell line***

508 For comparability, all BioID tags used in this study were generated using an identical cloning
509 strategy, incorporating an N-terminal HA tag for detection and a 3×(GGGS) linker between the tag
510 and the protein of interest, inserted C-terminally via Gateway cloning. The constructs have been
511 ordered as synthetic genes (Eurofins) and subcloned via *Eco*RI and *Xho*I into pcDNA3.0 (Invitrogen)
512 allowing the expression of fusion proteins in mammalian cells under the strong viral CMV promoter.
513 Gateway Destination clones were generated by cloning a Gateway cassette (Invitrogen) into an
514 *Eco*RV site at the 3' end and in frame of the different BioID-tags [BioID (Roux *et al*, 2012; referred as

515 BioID1), BioID2 (Kim *et al*, 2016), miniTurbo (Branon *et al*, 2018)]. For better and comparable
516 detection of the fusion proteins, all tags contained an N-terminal HA-tag. The LRRK2 expression
517 clones were subsequently generated by LR cloning (Invitrogen) based on ENTRY clones described
518 earlier (Gloeckner *et al*, 2010). The CDS of human of RAB29 was ordered as synthetic gene strand
519 (Eurofins) with flanking attB sites to allow its direct cloning into pDONR201 by BP cloning and
520 subsequently cloned into an in-house (N)FLAG-HA Gateway destination clone by the LR reaction. The
521 HEK293 cell line (ACC-305) stably expressing miniTurbo-LRRK2 was generated as previously
522 described (Gloeckner *et al*, 2007). Briefly, single colonies have been selected and tested after
523 transient transfection and selection via G418 (Sigma). The Flag-HA-CYLD vector was kindly provided
524 by Wade Harper (plasmid #22544, Addgene) (Sowa *et al*, 2009), the pCMV poly HA-Ubiquitin
525 construct was kindly provided by D. Bohmann (Treier *et al*, 1994) and the pRK5-HA-Ubiquitin-K63
526 vector was kindly provided by T. Dawson (plasmid #17606, Addgene) (Lim *et al*, 2005).

527 ***Cell culture and proximity labelling***

528 HEK293T (ACC-635) or HEK293 stably expressing miniTurbo-LRRK2 were grown in 14cm dishes in full
529 Dulbecco's modified medium (DMEM) supplemented with penicillin streptomycin and if not
530 mentioned otherwise with 10% FBS at 37°C in 5% CO2. The cells were grown for 8 h to 1 day
531 reaching a density of 50-80% until transfection with a self-made PEI (Polyethylenimine) reagent
532 (Guaitoli *et al*, 2016). For each condition, 4–6 plates were used. If not stated otherwise, for
533 biotinylation, cells have been incubated with 50 µM biotin (Sigma) in serum-free medium for up to
534 16 hours. In case of the mini turbo tag, cells have been incubated with 50 µM biotin for 2 h after o/n
535 starvation. Starvation was used to synchronize the cells and, in light of the physiological functions of
536 LRRK2, to enrich for post-mitotic states in which its centrosomal and ciliary roles are more
537 prominent. For the determination of the LRRK2-inhibitor dependent proximity proteomes, a HEK293
538 line stably expressing mT-LRRK2 was either incubated with 1 µM MLi-2, 1 µM GZD-824 or DMSO
539 (vehicle) 1h prior and during 2 h biotin incubation. For the analysis of RAB29-dependent proximity
540 proteomes, mT-LRRK2 was either co-expressed with HA-RAB29 or an empty pcDNA3.0 vector. See
541 also the point-to-point protocol deposited on Zenodo (DOI: 10.5281/zenodo.17045153).

542 ***Affinity purification of biotinylated proteins***

543 For cell lysis, cell culture dishes were transferred to ice and culture medium was removed. The cells
544 were rinsed two times with 5ml ice-cold PBS. The cells were covered with 1ml lysis buffer [1%
545 Nonidet P-40 Substitute (Merck), protease inhibitor cocktail (Roche), PhosSTOP (Roche) in TBS (30
546 mM Tris-HCl, pH7.4 and 150 mM NaCl)] per 14 cm dish and detached with a cell scraper. The cell
547 suspension was collected and incubated for 20-40 min on an end-over-end shaker at 4°C. Lysates

548 were cleared by centrifugation (15,000 x g for 10 min at 4°C). The protein concentration of cleared
549 lysates was determined photometrically using a nanodrop (Thermo-Fisher Scientific) or with the BCA
550 assay (Thermo-Fisher Scientific) following the manufacturer's instructions. Biotinylated proteins
551 were purified by affinity enrichment using either Strep-Tactin Superflow resin (IBA) or MagStrep
552 Strep-Tactin beads (IBA) in case of small-scale enrichments. To this end, the combined lysates for
553 each condition were incubated with an adjusted resin volume of 25 µl packed beads per 14cm cell
554 culture dish. The resin was equilibrated by washing 3-4x with 500 µl lysis buffer. The lysates were
555 incubated with the resin overnight at 4°C under constant agitation. After incubation, the resin was
556 sedimented by centrifugation at 1,000 x g for 3 min at 4°C. The supernatant was removed, leaving
557 approximately 300 µl to resuspend the resin. The resin suspension was transferred to microSpin
558 columns (Cytiva) and washed three times with 500 µl lysis buffer, followed by two washes with 500
559 µl 1x TBS (centrifugation for 5 s at 100 x g). Biotinylated proteins were eluted by incubation with
560 300-400 µl desthiobiotin elution buffer (2.5M, IBA). The desthiobiotin eluates were precipitated by
561 chloroform/ methanol and directly subjected to tryptic proteolysis following standard protocols
562 (Gloeckner *et al*, 2009) and stored at -80°C. The BioID protocol was further optimized during the
563 course of the study. A detailed step-by-step protocol has been deposited on Zenodo (DOI:
564 10.5281/zenodo.17045153). This protocol includes an additional SDS extraction step after cell lysis
565 and removal of nuclei and was used in particular for the inhibitor study.

566 ***CYLD co-expression experiment***

567 For the analysis of CYLD co-expression, cells were co-transfected with either Strep/FLAG (SF-TAP)-
568 tagged LRRK2 WT or LRRK2 Y1699C together with CYLD. As negative control, CYLD plasmid was
569 replaced by pCDNA3 empty vector, to maintain the plasmid concentration constant among the
570 different conditions. To test the influence of defined ubiquitin linkage types, ubiquitin—either in WT
571 form (pCMV poly HA-Ubiquitin) or K63 (pRK5-HA-Ubiquitin-K63)—was co-expressed. For
572 experiments relying on endogenous ubiquitin, the ubiquitin expression plasmids were replaced by
573 the pcDNA3 vector. The experiment was performed in 10 cm culture dishes. Cells were seeded at a
574 density of 3 to 4 million cells per dish and transfected the next day using home-made PEI
575 transfection reagent (cell confluency 30-40%). A total of 3.2 µg of plasmid DNA was used for each
576 plate. The plasmids ratios were LRRK2:CYLD:Ubiquitin 1:3:1. Cells were lysed 48 h post-transfection
577 (cell confluency approx. 80%) in 500 µl lysis buffer (see above) and incubated for 45 min at 4°C under
578 agitation. Cell debris was removed by centrifugation at 1,000 × g for 10 min at 4°C. To extract
579 membrane-bound prenylated proteins (e.g., Rab proteins), pre-cleared lysates were supplemented
580 with SDS (55 µl of a 10% stock solution) to a final concentration of 1% and incubated for 15 min at
581 4°C under agitation. Lysates were subsequently clarified by centrifugation at 20,000 × g for 10 min at

582 room temperature. Protein concentration was determined by BCA assay (Pierce), and LRRK2 levels
583 were assessed by capillary Western blotting (see below).

584 ***siRNA knockdown***

585 24h after splitting, cells were transfected with RNAiMAX (Life Technologies) following
586 manufacturer's instructions. The following siRNAs were used (Silencer Select®, Life Technologies):
587 PCM1 (#s10128, CAAAGACUCCACAUACGUUtt), Negative Control No. 2 (#4390846). 360 pmol of
588 siRNA were used for each technical replicate. Cells were kept in culture for another 48h before
589 proceeding with treatment with 10µM MLi-2 or DMSO. Cells were lysed as described above. Three
590 technical replicates for each condition (PCM1 or scrambled, MLi-2 or DMSO) were used. The effects
591 of PCM1 knockdown were evaluated via SDS-PAGE and Western Blot.

592 ***SDS PAGE and Western Blots***

593 For functional evaluation of the bait proteins and to determine the biotinylation efficiency, samples
594 were subjected to SDS PAGE and analyzed by Western-blotting on PVDF membranes. To assess
595 blotting efficiency and equal loading, the membranes were stained with Ponceau S. Prior to blocking
596 of the membranes in 5% nonfat dry milk powder (BioRad) or 1-5% BSA (Carl Roth) in TBS with 0.1%
597 Tween 20 (TBST) for 1-3h at RT, membranes were de-stained in TBST. Membranes were afterwards
598 incubated with primary antibody solutions overnight at 4°C under mild agitation. The following
599 primary antibodies were used: rat α-LRRK2 mAb (24D8 clone, hybridoma supernatant, generated in-
600 house (Carrion *et al*, 2017)) 1:1000 in 5% milk in TBST), rabbit α-pS935-LRRK2 mAb (Abcam,
601 ab133450; 1:100,000 in 5% BSA in TBST), rabbit α-RAB10 mAb (Abcam, ab181367; 1:5,000 in 5% milk
602 in TBST), rabbit α-pT73-RAB10 mAb (Abcam, ab230261; 1:1,000 in 5% BSA in TBST), rat α-HA-tag
603 (Roche, 3F10 clone, Rat 1gG1; 1:1,000 in 5% milk in TBST), mouse α-FLAG-tag (Sigma, F1804-200UG,
604 1:2,000 in 5% milk in TBST), rabbit α-PCM1 (Proteintech, 19856-1-AP, 1:24,000 in 5% milk in TBST),
605 mouse α-CYLD (Proteintech, 66858-1-Ig, 1:1,500 in 5% milk in TBST), rabbit α-SSX2IP (Thermo Fisher
606 Scientific, PA5-31495, 1:1,000 in 5% milk in TBST). Membranes were washed 5x 5min in TBST prior to
607 incubation with the HRP-conjugated secondary antibodies α-rat (Jackson Immuno-Research, 112-
608 036-062; 1:7,500), α-rabbit (Jackson Immuno-Research, 111-036-045; 1:7,500), and α-mouse
609 (Jackson Immuno-Research, 115-036-062; 1:7,500), respectively. For the detection of biotinylated
610 proteins, membranes were incubated with Pierce™ High Sensitivity Streptavidin-HRP (Thermo Fisher
611 Scientific, 1:20,000 in 1% BSA in TBST) overnight at 4°C and washed the next day 5x 5min in TBST.
612 Blots were developed with Pierce ECL Plus Western Blotting Substrate following the manufacturer's
613 protocol (Thermo Fisher Scientific) and exposed to Amersham Hyperfilm™ ECL (Cytiva). For
614 quantification of LRRK2 in presence of CYLD, the JESS capillary Western system (Biotechne) was

615 used. Separation was performed on a 25-capillary array (12-230kDa Fluorescence Separation; SM-
616 FL004-1) LRRK2 was detected by 24D8; 1:25/ rabbit anti-rat DyLight-633; 1:50 (Biotechne NBP1-
617 76225) in milk diluent. b-actin was detected by anti-b-actin; 1:500 (R&D Systems MAB8929)/ anti-
618 mouse-NIR (Biotechne 043-821); 1:20; in milk diluent. Detection for both proteins was done in the
619 NIR channel. Data analysis was performed using vendor software (Compass for SW, v7.1.0) and
620 custom Python scripts; graphical representations were generated with the Python library Seaborn.
621 Unpaired two-tailed t-tests were used to compare LRRK2 levels normalized by b-actin.

622 ***Mass spectrometry***

623 In solution proteolysis was performed as previously described (Gloeckner *et al*, 2009). Briefly,
624 chloroform/ methanol precipitates were dissolved in 50 mM ammonium bicarbonate pH8.0.
625 Cysteines were reduced and alkylated by treatment with 100 mM DTT and 300mM Iodoacetamide,
626 respectively following the incubation with trypsin (Sigma-Aldrich) overnight at 37°C. Samples were
627 desalted by micropipette C-18 solid-phase extraction tips (StageTip, Thermo Fisher Scientific) prior to
628 LC-MSMS analysis. Peptides were subsequently analyzed by LC-MSMS using a nanoflow HPLC system
629 (Ultimate 3000 RSLC; Thermo-Fisher Scientific) coupled to an Orbitrap Q-Exactive plus (Thermo
630 Fisher Scientific) tandem mass spectrometer. Peptides were separated by reversed C-18
631 chromatography and 120-minute gradients. MS1 spectra were acquired in the Orbitrap at 70K
632 resolution. After selection of the 10 most intense precursor ions from the MS1 scans for HCD
633 fragmentation (Top 10 method), MS2 spectra were acquired at 17.5K. RAW MS files were analyzed
634 with Maxquant (version 2.0.3.1), enabling label-free-quantification (LFQ with no normalization) and
635 "match between runs" (Cox *et al*, 2014). For the embedded Andromeda search engine, trypsin has
636 been selected as enzyme and carbamylation was set as fixed modification N-terminal acetylation
637 was set as variable modification. The search was performed against the human subset of the
638 Uniprot/Swissprot database (release 2021_04, 20375 entries). The MaxQuant output was further
639 processed by Perseus and SaintExpress.

640 ***Perseus post-processing***

641 For post-analysis, the protein groups were further processed by Perseus (v. 1.6.7). LFQ intensities of
642 the individual were assigned to the conditions and potential contaminants, reverse hits as well as IDs
643 only identified by site were filtered out. For further analysis, only IDs with a maximum number of
644 missing values of n-1 in at least one condition were considered. Remaining missing values were
645 replaced by group-wise imputation based on a normal distribution (log2 values) around the
646 detection limit (width=0.3; down-shift=1.8). Intensities of the individual experiments were
647 normalized by their medians and significantly enriched proteins (condition vs control) were

648 determined by a moderated permutation-based T-test (FDR = 0.05, S0 = 0.1) as implemented in
649 Perseus (Two-sample test).

650 ***SaintExpress post-processing***

651 We followed a previously described protocol (Liu *et al*, 2020; see also http://proteomics.fi) to select
652 the most confident interactors using the statistical framework of SAINTExpress (Teo *et al*, 2014), as
653 well as a reference knowledgebase for contaminants (i.e. CRAPome (Mellacheruvu *et al*, 2013)), to
654 filter out most likely false negative interactors. In particular, we generated the "Bait", "Prey" and
655 "Interaction" files to be subjected to the analysis pipeline from the MaxQuant "*proteinGroups.txt*"
656 file by employing the following columns: "Bait" file (IP name = EV_* or LRRK2_*, bait name = LRRK2,
657 indicator for test and negative control= C = EV_*, T = LRRK2_*); "Interaction" file (IP name =
658 EV_*/LRRK_*, bait name = LRRK2, prey name = interaction partner gene symbol, spectral count or
659 intensity values = LFQ intensity); "Prey" file (prey (protein)name = interaction partner Uniprot
660 accession, prey protein length=Sequence length, prey gene name = gene symbol). The proteins that
661 were not classified through the CRAPome filter, were retained together with those passing the filter.

662 We unified the interactor list from the three BioID experiments. Finally, we retained a list of 208
663 interactors which passed the two filters. Only 45 proteins in the filtered interactor list are already
664 present in IntAct.

665 ***Graphical representation and network annotation***

666 PPI networks were analyzed by Cytoscape version 3.8.2 (Shannon *et al*, 2003) and were mapped to
667 available interaction from IntAct using the Cytoscape IntAct app (Ragueneau *et al*, 2021). Networks
668 were annotated with STRINGDB terms via the 'Stringify' function of the StringApp (Doncheva *et al*,
669 2019) and functional enrichment retrieved via the same app. We annotated the networks with the
670 AutoAnnotate plug-in (Kucera *et al*, 2016), using the GLay clustering method, and generated the
671 cluster labels with the Adjacent Words option of the WordCloud algorithm, based on significantly
672 enriched GO Biological Process and Cellular Component terms associated with the genes in each
673 network. The Venn diagram shown in Figure 1A has been generated with JVenn provided by the
674 ProteoRE server (Galaxy Version 2021.05.12) (Galaxy, 2024).

675 **Co-evolution based PPI stratification**

676 Co-evolution of two proteins A and B was measured as the Jaccard similarity coefficient of the set of
677 genomes containing an orthologous sequence of A and the set of genomes containing an
678 orthologous sequence of B. Orthologous sequences were collected from the Orthologous MAtrix

679 (OMA) database (Altenhoff *et al*, 2021) using a Python script written in-house using the PyOMADB
680 client (Kaleb *et al*, 2019) (Kaleb *et al*, 2019) (December 13, 2023, database version July 2023).

681 **AF-multimer prediction of binary interactions**

682 We used Alphafold-Multimer v2.3.2 (preprint: Evans *et al*, 2021) to generate 3D models of full-length
683 LRRK2 binary interaction complexes for all the interactors shorter than 2000 residues. The databases
684 required to run AlphaFold-Multimer were downloaded on 12 January 2023 and the predictions were
685 run with the flag –max template date = 01-01-1900, to avoid the usage of any available experimental
686 templates. Among the 5 models generated for each LRRK2 binary complex, only the best one was
687 considered for further analysis. The score used to evaluate the models was the default one used by
688 AlphaFold-Multimer (0.2*pTM + 0.8*ipTM).

689 **Interaction fingerprint**

690 AlphaFold produces probabilities for the $C_ß$-$C_ß$ distances between residues *i* and *j* to fall into a series
691 of distance bins. For each pair of residues, we calculated the expected value of such distance
692 distribution, yielding a matrix of dimension l_{LRRK2} x l_n, corresponding to the sequence lengths of
693 LRRK2 and the *n*th interacting partner, respectively. Subsequently, we pooled the distogram on the
694 interaction partner's side and we assigned to each residue of LRRK2 the minimum expected distance
695 to any residue of the interactor. We refer to this vector of minimum expected distances as the
696 interaction fingerprint of a given interacting protein.

697 **RMSD calculation**

698 We compared LRRK2 conformations by performing Root Mean Square Deviation (RMSD)-based
699 clustering. To calculate the RMSD we fitted the structures using the C_α atoms of the LRRK2 chains
700 from position 983 to the end of the sequence. The N-terminal portion of the protein was excluded
701 because it is very flexible. Calculations were performed using the Superimposer function of the PDB
702 Biopython module (Cock *et al*, 2009) (version 1.83) through customized scripts and pipeline (Matic *et*
703 *al*, 2023).

704 **Clustering**

705 The clustering was performed using the Ward method with the *clustermap* function from *seaborn*
706 python library (version 0.11.2). Results were displayed through matplotlib (https://matplotlib.org/)
707 and seaborn (https://seaborn.pydata.org/) libraries using customized python scripts. The number of
708 clusters chosen was one that maximized the mean Silhouette Coefficient of all samples (Rousseeuw,
709 1987), as computed by the *silhouette_score* function in *scikit-learn* (Pedregosa *et al*, 2011).

710 **Data availability**

711 The mass spectrometry proteomics data have been deposited to the ProteomeXchange Consortium
712 via the PRIDE (Perez-Riverol *et al*, 2022) partner repository with the dataset identifier PXD048832
713 and https://doi.org/10.6019/PXD048832 (BioID1, BioID2, miniTurbo), PXD048806 and
714 https://doi.org/10.6019/PXD048806 (LRRK2 proximity-proteomes MLi-2 vs. GZD-524) as well as
715 PXD048808 and https://doi.org/10.6019/PXD048808 (RAB29 co-expression). The BioID interaction
716 network and associated co-evolutionary and structural analysis can be accessed at the following
717 URL: (https://dip.bioinfolab.sns.it/explore/). The code used for the analysis is available at the
718 following links: https://github.com/raimondilab/distogram_analysis,
719 https://github.com/raimondilab/Stable_complex_predictor. A point-to-point protocol for the BioID
720 approach was deposited on Zenodo (DOI: 10.5281/zenodo.17045153).

721 **Acknowledgments**

722 We are grateful to the staff of the Core Facility for Medical Proteomics at the medical faculty of the
723 University of Tübingen for technical assistance. Furthermore, we gratefully acknowledge
724 computational resources of the Center for High Performance Computing (CHPC) at SNS. CJG received
725 funds from The Michael J. Fox Foundation for Parkinson's Research (grant ID: MJFF-8068.02, MJFF-
726 8068.04 and MJFF-023920) and iMed – the Helmholtz Initiative on Personalized Medicine.

727 **Disclosure and competing interest statement**

728 The authors declare that they have no competing interests.

729 **Limitations of the study**

730 While the HEK293T system enables large-scale experimental throughput, it may exhibit a cell-type–
731 specific bias, including an overrepresentation of microtubule-binding proteins compared with other
732 cell types. Another limitation is the low endogenous expression of LRRK2 in HEK293T cells. As a
733 result, the study relies on the overexpression of LRRK2 BioID fusion proteins, which may introduce
734 artifacts not present under physiological conditions.

735 **References**

736 Almawi AW, Matthews LA, Guarne A (2017) FHA domains: Phosphopeptide binding and beyond.
737 *Prog Biophys Mol Biol* 127: 105-110
738 Altenhoff AM, Train CM, Gilbert KJ, Mediratta I, Mendes de Farias T, Moi D, Nevers Y, Radoykova HS,
739 Rossier V, Warwick Vesztrocy A *et al* (2021) OMA orthology in 2021: website overhaul,
740 conserved isoforms, ancestral gene order and more. *Nucleic acids research* 49: D373-D379
741 Bang Y, Kim KS, Seol W, Choi HJ (2016) LRRK2 interferes with aggresome formation for autophagic
742 clearance. *Mol Cell Neurosci* 75: 71-80
743 Barenz F, Inoue D, Yokoyama H, Tegha-Dunghu J, Freiss S, Draeger S, Mayilo D, Cado I, Merker S,
744 Klinger M *et al* (2013) The centriolar satellite protein SSX2IP promotes centrosome
745 maturation. *J Cell Biol* 202: 81-95
746 Beilina A, Rudenko IN, Kaganovich A, Civiero L, Chau H, Kalia SK, Kalia LV, Lobbestael E, Chia R,
747 Ndukwe K *et al* (2014) Unbiased screen for interactors of leucine-rich repeat kinase 2
748 supports a common pathway for sporadic and familial Parkinson disease. *Proceedings of the*
749 *National Academy of Sciences of the United States of America* 111: 2626-2631
750 Bersuker K, Peterson CWH, To M, Sahl SJ, Savikhin V, Grossman EA, Nomura DK, Olzmann JA (2018) A
751 Proximity Labeling Strategy Provides Insights into the Composition and Dynamics of Lipid
752 Droplet Proteomes. *Dev Cell* 44: 97-112 e117
753 Boecker CA, Holzbaur ELF (2021) Hyperactive LRRK2 kinase impairs the trafficking of axonal
754 autophagosomes. *Autophagy* 17: 2043-2045
755 Boldt K, van Reeuwijk J, Lu Q, Koutroumpas K, Nguyen TM, Texier Y, van Beersum SE, Horn N, Willer
756 JR, Mans DA *et al* (2016) An organelle-specific protein landscape identifies novel diseases
757 and molecular mechanisms. *Nature communications* 7: 11491
758 Bonet-Ponce L, Beilina A, Williamson CD, Lindberg E, Kluss JH, Saez-Atienzar S, Landeck N, Kumaran
759 R, Mamais A, Bleck CKE *et al* (2020) LRRK2 mediates tubulation and vesicle sorting from
760 lysosomes. *Sci Adv* 6
761 Branon TC, Bosch JA, Sanchez AD, Udeshi ND, Svinkina T, Carr SA, Feldman JL, Perrimon N, Ting AY
762 (2018) Efficient proximity labeling in living cells and organisms with TurboID. *Nat Biotechnol*
763 36: 880-887
764 Carrion MDP, Marsicano S, Daniele F, Marte A, Pischedda F, Di Cairano E, Piovesana E, von Zweydorf
765 F, Kremmer E, Gloeckner CJ *et al* (2017) The LRRK2 G2385R variant is a partial loss-of-
766 function mutation that affects synaptic vesicle trafficking through altered protein
767 interactions. *Sci Rep* 7: 5377
768 Chen C, Xu Z, Zhang T, Lin L, Lu M, Xie C, Yu X (2019) Cep85 Relays Plk1 Activity to Phosphorylated
769 Nek2A for Its Timely Activation in Centrosome Disjunction. *iScience* 11: 114-133
770 Cock PJ, Antao T, Chang JT, Chapman BA, Cox CJ, Dalke A, Friedberg I, Hamelryck T, Kauff F,
771 Wilczynski B *et al* (2009) Biopython: freely available Python tools for computational
772 molecular biology and bioinformatics. *Bioinformatics* 25: 1422-1423
773 Cox J, Hein MY, Luber CA, Paron I, Nagaraj N, Mann M (2014) Accurate proteome-wide label-free
774 quantification by delayed normalization and maximal peptide ratio extraction, termed
775 MaxLFQ. *Molecular & cellular proteomics : MCP* 13: 2513-2526
776 Dammermann A, Merdes A (2002) Assembly of centrosomal proteins and microtubule organization
777 depends on PCM-1. *J Cell Biol* 159: 255-266
778 Deniston CK, Salogiannis J, Mathea S, Snead DM, Lahiri I, Matyszewski M, Donosa O, Watanabe R,
779 Bohning J, Shiau AK *et al* (2020) Structure of LRRK2 in Parkinson's disease and model for
780 microtubule interaction. *Nature* 588: 344-349
781 Dhekne HS, Tonelli F, Yeshaw WM, Chiang CY, Limouse C, Jaimon E, Purlyte E, Alessi DR, Pfeffer SR
782 (2023) Genome-wide screen reveals Rab12 GTPase as a critical activator of Parkinson's
783 disease-linked LRRK2 kinase. *Elife* 12

784 Dhekne HS, Yanatori I, Gomez RC, Tonelli F, Diez F, Schule B, Steger M, Alessi DR, Pfeffer SR (2018) A
785 pathway for Parkinson's Disease LRRK2 kinase to block primary cilia and Sonic hedgehog
786 signaling in the brain. *Elife* 7
787 Dobson-Stone C, Hallupp M, Shahheydari H, Ragagnin AMG, Chatterton Z, Carew-Jones F, Shepherd
788 CE, Stefen H, Paric E, Fath T *et al* (2020) CYLD is a causative gene for frontotemporal
789 dementia - amyotrophic lateral sclerosis. *Brain* 143: 783-799
790 Doncheva NT, Morris JH, Gorodkin J, Jensen LJ (2019) Cytoscape StringApp: Network Analysis and
791 Visualization of Proteomics Data. *Journal of proteome research* 18: 623-632
792 Douanne T, Andre-Gregoire G, Thys A, Trillet K, Gavard J, Bidere N (2019) CYLD Regulates Centriolar
793 Satellites Proteostasis by Counteracting the E3 Ligase MIB1. *Cell Rep* 27: 1657-1665 e1654
794 Eguether T, Ermolaeva MA, Zhao Y, Bonnet MC, Jain A, Pasparakis M, Courtois G, Tassin AM (2014)
795 The deubiquitinating enzyme CYLD controls apical docking of basal bodies in ciliated
796 epithelial cells. *Nature communications* 5: 4585
797 Ehebauer MT, Arias AM (2009) The structural and functional determinants of the Axin and
798 Dishevelled DIX domains. *BMC Struct Biol* 9: 70
799 Evans R, O'Neill M, Pritzel A, Antropova N, Senior A, Green T, Žídek A, Bates R, Blackwell S, Yim J *et al*
800 (2021) Protein complex prediction with AlphaFold-Multimer. *bioRxiv* doi:
801 10.1101/2021.10.04.463034 [PREPRINT]
802 Fahn S (2003) Description of Parkinson's disease as a clinical syndrome. *Annals of the New York*
803 *Academy of Sciences* 991: 1-14
804 Filippini F, Nola S, Zahraoui A, Roger K, Esmaili M, Sun J, Wojnacki J, Vlieghe A, Bun P, Blanchon S *et*
805 *al* (2023) Secretion of VGF relies on the interplay between LRRK2 and post-Golgi v-SNAREs.
806 *Cell Rep* 42: 112221
807 Follett J, Farrer MJ (2021) LRRK2; a dynamic regulator of cellular trafficking. *Brain Res* 1761: 147394
808 Galaxy C (2024) The Galaxy platform for accessible, reproducible, and collaborative data analyses:
809 2024 update. *Nucleic acids research* 52: W83-W94
810 Gasser T, Hardy J, Mizuno Y (2011) Milestones in PD genetics. *Mov Disord* 26: 1042-1048
811 Geisler S, Holmstrom KM, Skujat D, Fiesel FC, Rothfuss OC, Kahle PJ, Springer W (2010) PINK1/Parkin-
812 mediated mitophagy is dependent on VDAC1 and p62/SQSTM1. *Nat Cell Biol* 12: 119-131
813 Gloeckner CJ, Boldt K, Schumacher A, Roepman R, Ueffing M (2007) A novel tandem affinity
814 purification strategy for the efficient isolation and characterisation of native protein
815 complexes. *Proteomics* 7: 4228-4234
816 Gloeckner CJ, Boldt K, Ueffing M (2009) Strep/FLAG tandem affinity purification (SF-TAP) to study
817 protein interactions. *Current protocols in protein science / editorial board, John E Coligan [et*
818 *al]* Chapter 19: Unit19 20
819 Gloeckner CJ, Boldt K, von Zweydorf F, Helm S, Wiesent L, Sarioglu H, Ueffing M (2010)
820 Phosphopeptide analysis reveals two discrete clusters of phosphorylation in the N-terminus
821 and the Roc domain of the Parkinson-disease associated protein kinase LRRK2. *Journal of*
822 *proteome research* 9: 1738-1745
823 Gloeckner CJ, Porras P (2020) Guilt-by-Association - Functional Insights Gained From Studying the
824 LRRK2 Interactome. *Front Neurosci* 14: 485
825 Grishin NV (2001) KH domain: one motif, two folds. *Nucleic acids research* 29: 638-643
826 Guaitoli G, Raimondi F, Gilsbach BK, Gomez-Llorente Y, Deyaert E, Renzi F, Li X, Schaffner A, Jagtap
827 PK, Boldt K *et al* (2016) Structural model of the dimeric Parkinson's protein LRRK2 reveals a
828 compact architecture involving distant interdomain contacts. *Proceedings of the National*
829 *Academy of Sciences of the United States of America* 113: E4357-4366
830 Guaitoli G, Zhang X, Saitta F, Miglionico P, Silbermann LM, Ho FY, von Zweydorf F, Signorelli M, Tych
831 K, Fessas D *et al* (2023) Biophysical analysis reveals autophosphorylation as an important
832 regulator of LRRK2 dimerization. *bioRxiv* doi: 10.1101/2023.08.11.549911 [PREPRINT]

833 Hall EA, Kumar D, Prosser SL, Yeyati PL, Herranz-Perez V, Garcia-Verdugo JM, Rose L, McKie L, Dodd
834 DO, Tennant PA *et al* (2023) Centriolar satellites expedite mother centriole remodeling to
835 promote ciliogenesis. *Elife* 12
836 Hallett PJ, Engelender S, Isacson O (2019) Lipid and immune abnormalities causing age-dependent
837 neurodegeneration and Parkinson's disease. *J Neuroinflammation* 16: 153
838 Hori A, Toda T (2017) Regulation of centriolar satellite integrity and its physiology. *Cellular and*
839 *molecular life sciences : CMLS* 74: 213-229
840 Islam MS, Nolte H, Jacob W, Ziegler AB, Putz S, Grosjean Y, Szczepanowska K, Trifunovic A, Braun T,
841 Heumann H *et al* (2016) Human R1441C LRRK2 regulates the synaptic vesicle proteome and
842 phosphoproteome in a Drosophila model of Parkinson's disease. *Human molecular genetics*
843 25: 5365-5382
844 Jennings D, Huntwork-Rodriguez S, Henry AG, Sasaki JC, Meisner R, Diaz D, Solanoy H, Wang X,
845 Negrou E, Bondar VV *et al* (2022) Preclinical and clinical evaluation of the LRRK2 inhibitor
846 DNL201 for Parkinson's disease. *Science translational medicine* 14: eabj2658
847 Jian F, Wang S, Tian R, Wang Y, Li C, Li Y, Wang S, Fang C, Ma C, Rong Y (2024) The STX17-SNAP47-
848 VAMP7/VAMP8 complex is the default SNARE complex mediating autophagosome-lysosome
849 fusion. *Cell Res*
850 Kafka A, Basic-Kinda S, Pecina-Slaus N (2014) The cellular story of dishevelleds. *Croat Med J* 55: 459-
851 467
852 Kaleb K, Vesztrocy AW, Altenhoff A, Dessimoz C (2019) Expanding the Orthologous Matrix (OMA)
853 programmatic interfaces: REST API and the OmaDB packages for R and Python. *F1000Res* 8:
854 42
855 Kalogeropulou AF, Purlyte E, Tonelli F, Lange SM, Wightman M, Prescott AR, Padmanabhan S,
856 Sammler E, Alessi DR (2022) Impact of 100 LRRK2 variants linked to Parkinson's Disease on
857 kinase activity and microtubule binding. *The Biochemical journal*
858 Kalogeropulou AF, Zhao J, Bolliger MF, Memou A, Narasimha S, Molitor TP, Wilson WH, Rideout HJ,
859 Nichols RJ (2018) P62/SQSTM1 is a novel leucine-rich repeat kinase 2 (LRRK2) substrate that
860 enhances neuronal toxicity. *The Biochemical journal* 475: 1271-1293
861 Kanao T, Venderova K, Park DS, Unterman T, Lu B, Imai Y (2010) Activation of FoxO by LRRK2 induces
862 expression of proapoptotic proteins and alters survival of postmitotic dopaminergic neuron
863 in Drosophila. *Human molecular genetics* 19: 3747-3758
864 Khan SS, Jaimon E, Lin YE, Nikoloff J, Tonelli F, Alessi DR, Pfeffer SR (2024) Loss of primary cilia and
865 dopaminergic neuroprotection in pathogenic LRRK2-driven and idiopathic Parkinson's
866 disease. *Proceedings of the National Academy of Sciences of the United States of America*
867 121: e2402206121
868 Kim DI, Jensen SC, Noble KA, Kc B, Roux KH, Motamedchaboki K, Roux KJ (2016) An improved smaller
869 biotin ligase for BioID proximity labeling. *Mol Biol Cell* 27: 1188-1196
870 Kluss JH, Bonet-Ponce L, Lewis PA, Cookson MR (2022a) Directing LRRK2 to membranes of the
871 endolysosomal pathway triggers RAB phosphorylation and JIP4 recruitment. *Neurobiol Dis*
872 170: 105769
873 Kluss JH, Lewis PA, Greggio E (2022b) Leucine-rich repeat kinase 2 (LRRK2): an update on the
874 potential therapeutic target for Parkinson's disease. *Expert Opin Ther Targets* 26: 537-546
875 Kucera M, Isserlin R, Arkhangorodsky A, Bader GD (2016) AutoAnnotate: A Cytoscape app for
876 summarizing networks with semantic annotations. *F1000Res* 5: 1717
877 Kumar M, Acevedo-Cintron J, Jhaldiyal A, Wang H, Andrabi SA, Eacker S, Karuppagounder SS,
878 Brahmachari S, Chen R, Kim H *et al* (2020) Defects in Mitochondrial Biogenesis Drive
879 Mitochondrial Alterations in PARKIN-Deficient Human Dopamine Neurons. *Stem Cell Reports*
880 15: 629-645
881 Lara Ordonez AJ, Fasiczka R, Fernandez B, Naaldijk Y, Fdez E, Blanca Ramirez M, Phan S, Boassa D,
882 Hilfiker S (2022) The LRRK2 signaling network converges on a centriolar phospho-

883 Rab10/RILPL1 complex to cause deficits in centrosome cohesion and cell polarization. *Biol*
884 *Open* 11
885 Lara Ordonez AJ, Fernandez B, Fdez E, Romo-Lozano M, Madero-Perez J, Lobbestael E, Baekelandt V,
886 Aiastui A, Lopez de Munain A, Melrose HL *et al* (2019) RAB8, RAB10 and RILPL1 contribute to
887 both LRRK2 kinase-mediated centrosomal cohesion and ciliogenesis deficits. *Human*
888 *molecular genetics* 28: 3552-3568
889 Li BJ, Chen H, Jiang SS, Wang CY, Tuo QH, Long SY, Zhang CP, Liao DF (2020) PX Domain-Containing
890 Kinesin KIF16B and Microtubule-Dependent Intracellular Movements. *J Membr Biol* 253:
891 101-108
892 Li P, Li J, Wang L, Di LJ (2017) Proximity Labeling of Interacting Proteins: Application of BioID as a
893 Discovery Tool. *Proteomics* 17
894 Li X, Zhu H, Huang BT, Li X, Kim H, Tan H, Zhang Y, Choi I, Peng J, Xu P *et al* (2024) RAB12-LRRK2
895 complex suppresses primary ciliogenesis and regulates centrosome homeostasis in
896 astrocytes. *Nature communications* 15: 8434
897 Lim KL, Chew KC, Tan JM, Wang C, Chung KK, Zhang Y, Tanaka Y, Smith W, Engelender S, Ross CA *et*
898 *al* (2005) Parkin mediates nonclassical, proteasomal-independent ubiquitination of
899 synphilin-1: implications for Lewy body formation. *J Neurosci* 25: 2002-2009
900 Liu X, Salokas K, Weldatsadik RG, Gawriyski L, Varjosalo M (2020) Combined proximity labeling and
901 affinity purification-mass spectrometry workflow for mapping and visualizing protein
902 interaction networks. *Nature protocols* 15: 3182-3211
903 Lobbestael E, Civiero L, De Wit T, Taymans JM, Greggio E, Baekelandt V (2016) Pharmacological
904 LRRK2 kinase inhibition induces LRRK2 protein destabilization and proteasomal degradation.
905 *Sci Rep* 6: 33897
906 Manzoni C, Denny P, Lovering RC, Lewis PA (2015) Computational analysis of the LRRK2 interactome.
907 *PeerJ* 3: e778
908 Matic M, Miglionico P, Tatsumi M, Inoue A, Raimondi F (2023) GPCRome-wide analysis of G-protein-
909 coupling diversity using a computational biology approach. *Nature communications* 14: 4361
910 McGrath E, Waschbusch D, Baker BM, Khan AR (2021) LRRK2 binds to the Rab32 subfamily in a GTP-
911 dependent manner via its armadillo domain. *Small GTPases* 12: 133-146
912 Meixner A, Boldt K, Van Troys M, Askenazi M, Gloeckner CJ, Bauer M, Marto JA, Ampe C, Kinkl N,
913 Ueffing M (2011) A QUICK screen for Lrrk2 interaction partners--leucine-rich repeat kinase 2
914 is involved in actin cytoskeleton dynamics. *Molecular & cellular proteomics : MCP* 10: M110
915 001172
916 Meldal BHM, Perfetto L, Combe C, Lubiana T, Ferreira Cavalcante JV, Bye AJH, Waagmeester A, Del-
917 Toro N, Shrivastava A, Barrera E *et al* (2022) Complex Portal 2022: new curation frontiers.
918 *Nucleic acids research* 50: D578-D586
919 Mellacheruvu D, Wright Z, Couzens AL, Lambert JP, St-Denis NA, Li T, Miteva YV, Hauri S, Sardiu ME,
920 Low TY *et al* (2013) The CRAPome: a contaminant repository for affinity purification-mass
921 spectrometry data. *Nature methods* 10: 730-736
922 Miglionico P, Nemati Fard LA, Gloeckner CJ, Raimondi F (2024) Predicition and discovery of protein-
923 protein direct interactions and stable complexes based on gene co-expression and co-
924 evolution. *bioRxiv* doi: 10.1101/2024.10.05.616780 [PREPRINT]
925 Miller GK, Kuruvilla S, Jacob B, LaFranco-Scheuch L, Bakthavatchalu V, Flor J, Flor K, Ziegler J,
926 Reichard C, Manfre P *et al* (2023) Effects of LRRK2 Inhibitors in Nonhuman Primates. *Toxicol*
927 *Pathol*: 1926233231205895
928 Mohd Rafiq N, Fujise K, Rosenfeld MS, Xu P, De Camilli P (2024) Parkinsonism Sac domain mutation
929 in Synaptojanin-1 affects ciliary properties in iPSC-derived dopaminergic neurons.
930 *Proceedings of the National Academy of Sciences of the United States of America* 121:
931 e2318943121
932 Moreira C, Kelemen CD, Obado SO, Zahedifard F, Zhang N, Holetz FB, Gauglitz L, Dallagiovanna B,
933 Field MC, Kramer S *et al* (2023) Impact of inherent biases built into proteomic techniques:

934 Proximity labeling and affinity capture compared. *The Journal of biological chemistry* 299:
935 102726
936 Myasnikov A, Zhu H, Hixson P, Xie B, Yu K, Pitre A, Peng J, Sun J (2021) Structural analysis of the full-
937 length human LRRK2. *Cell* 184: 3519-3527 e3510
938 Naaldijk Y, Fernandez B, Fasiczka R, Fdez E, Leghay C, Croitoru I, Kwok JB, Boulesnane Y, Vizeneux A,
939 Mutez E *et al* (2024) A potential patient stratification biomarker for Parkinson s disease
940 based on LRRK2 kinase-mediated centrosomal alterations in peripheral blood-derived cells.
941 *NPJ Parkinsons Dis* 10: 12
942 Orchard S, Ammari M, Aranda B, Breuza L, Briganti L, Broackes-Carter F, Campbell NH, Chavali G,
943 Chen C, del-Toro N *et al* (2014) The MIntAct project--IntAct as a common curation platform
944 for 11 molecular interaction databases. *Nucleic acids research* 42: D358-363
945 Paisan-Ruiz C, Jain S, Evans EW, Gilks WP, Simon J, van der Brug M, Lopez de Munain A, Aparicio S,
946 Gil AM, Khan N *et al* (2004) Cloning of the gene containing mutations that cause PARK8-
947 linked Parkinson's disease. *Neuron* 44: 595-600
948 Park S, Han S, Choi I, Kim B, Park SP, Joe EH, Suh YH (2016) Interplay between Leucine-Rich Repeat
949 Kinase 2 (LRRK2) and p62/SQSTM-1 in Selective Autophagy. *PloS one* 11: e0163029
950 Pedregosa F, Varoquaux G, Gramfort A, Michel V, B. T, Griesel O, Blondel M, Prettenhofer P, Weiss R,
951 Dubourg V *et al* (2011) Scikit-learn: Machine Learning in Python. *Journal of Machine Learning*
952 *Research* 12: 2825-2830
953 Perez-Riverol Y, Bai J, Bandla C, Garcia-Seisdedos D, Hewapathirana S, Kamatchinathan S, Kundu DJ,
954 Prakash A, Frericks-Zipper A, Eisenacher M *et al* (2022) The PRIDE database resources in
955 2022: a hub for mass spectrometry-based proteomics evidences. *Nucleic acids research* 50:
956 D543-D552
957 Piccoli G, Condliffe SB, Bauer M, Giesert F, Boldt K, De Astis S, Meixner A, Sarioglu H, Vogt-
958 Weisenhorn DM, Wurst W *et al* (2011) LRRK2 controls synaptic vesicle storage and
959 mobilization within the recycling pool. *J Neurosci* 31: 2225-2237
960 Piccoli G, Onofri F, Cirnaru MD, Kaiser CJ, Jagtap P, Kastenmuller A, Pischedda F, Marte A, von
961 Zweydorf F, Vogt A *et al* (2014) Leucine-rich repeat kinase 2 binds to neuronal vesicles
962 through protein interactions mediated by its C-terminal WD40 domain. *Mol Cell Biol* 34:
963 2147-2161
964 Pirooznia SK, Wang H, Panicker N, Kumar M, Neifert S, Dar MA, Lau E, Kang BG, Redding-Ochoa J,
965 Troncoso JC *et al* (2022) Deubiquitinase CYLD acts as a negative regulator of dopamine
966 neuron survival in Parkinson's disease. *Sci Adv* 8: eabh1824
967 Prosser SL, Tkach J, Gheiratmand L, Kim J, Raught B, Morrison CG, Pelletier L (2022) Aggresome
968 assembly at the centrosome is driven by CP110-CEP97-CEP290 and centriolar satellites. *Nat*
969 *Cell Biol* 24: 483-496
970 Purlyte E, Dhekne HS, Sarhan AR, Gomez R, Lis P, Wightman M, Martinez TN, Tonelli F, Pfeffer SR,
971 Alessi DR (2018) Rab29 activation of the Parkinson's disease-associated LRRK2 kinase. *The*
972 *EMBO journal* 37: 1-18
973 Qin W, Cho KF, Cavanagh PE, Ting AY (2021) Deciphering molecular interactions by proximity
974 labeling. *Nature methods* 18: 133-143
975 Ragueneau E, Shrivastava A, Morris JH, Del-Toro N, Hermjakob H, Porras P (2021) IntAct App: a
976 Cytoscape application for molecular interaction network visualization and analysis.
977 *Bioinformatics* 37: 3684-3685
978 Raig ND, Surridge KJ, Sanz-Murillo M, Dederer V, Kramer A, Schwalm MP, Lattal NM, Elson L,
979 Chatterjee D, Mathea S *et al* (2025) Type II kinase inhibitors that target Parkinson's disease-
980 associated LRRK2. *Sci Adv* 11: eadt2050
981 Rousseeuw PJ (1987) Silhouettes: A graphical aid to the interpretation and validation of cluster
982 analysis. *Journal of Computational and Applied Mathematics* 20: 53-65
983 Roux KJ, Kim DI, Raida M, Burke B (2012) A promiscuous biotin ligase fusion protein identifies
984 proximal and interacting proteins in mammalian cells. *J Cell Biol* 196: 801-810

985 Sancho RM, Law BM, Harvey K (2009) Mutations in the LRRK2 Roc-COR tandem domain link
986 Parkinson's disease to Wnt signalling pathways. *Human molecular genetics* 18: 3955-3968
987 Schmidt S, Luecken MD, Trumbach D, Hembach S, Niedermeier KM, Wenck N, Pflugler K, Stautner C,
988 Bottcher A, Lickert H *et al* (2022) Primary cilia and SHH signaling impairments in human and
989 mouse models of Parkinson's disease. *Nature communications* 13: 4819
990 Shannon P, Markiel A, Ozier O, Baliga NS, Wang JT, Ramage D, Amin N, Schwikowski B, Ideker T
991 (2003) Cytoscape: a software environment for integrated models of biomolecular interaction
992 networks. *Genome Res* 13: 2498-2504
993 Shin WH, Park JH, Chung KC (2020) The central regulator p62 between ubiquitin proteasome system
994 and autophagy and its role in the mitophagy and Parkinson's disease. *BMB Rep* 53: 56-63
995 Simon-Sanchez J, Schulte C, Bras JM, Sharma M, Gibbs JR, Berg D, Paisan-Ruiz C, Lichtner P, Scholz
996 SW, Hernandez DG *et al* (2009) Genome-wide association study reveals genetic risk
997 underlying Parkinson's disease. *Nat Genet* 41: 1308-1312
998 Sowa ME, Bennett EJ, Gygi SP, Harper JW (2009) Defining the human deubiquitinating enzyme
999 interaction landscape. *Cell* 138: 389-403
1000 Steger M, Diez F, Dhekne HS, Lis P, Nirujogi RS, Karayel O, Tonelli F, Martinez TN, Lorentzen E, Pfeffer
1001 SR *et al* (2017) Systematic proteomic analysis of LRRK2-mediated Rab GTPase
1002 phosphorylation establishes a connection to ciliogenesis. *Elife* 6
1003 Stevens DA, Lee Y, Kang HC, Lee BD, Lee YI, Bower A, Jiang H, Kang SU, Andrabi SA, Dawson VL *et al*
1004 (2015) Parkin loss leads to PARIS-dependent declines in mitochondrial mass and respiration.
1005 *Proceedings of the National Academy of Sciences of the United States of America* 112:
1006 11696-11701
1007 Tasegian A, Singh F, Ganley IG, Reith AD, Alessi DR (2021) Impact of Type II LRRK2 inhibitors on
1008 signaling and mitophagy. *The Biochemical journal* 478: 3555-3573
1009 Taylor SS, Kaila-Sharma P, Weng JH, Aoto P, Schmidt SH, Knapp S, Mathea S, Herberg FW (2020)
1010 Kinase Domain Is a Dynamic Hub for Driving LRRK2 Allostery. *Frontiers in molecular*
1011 *neuroscience* 13: 538219
1012 Teo G, Liu G, Zhang J, Nesvizhskii AI, Gingras AC, Choi H (2014) SAINTexpress: improvements and
1013 additional features in Significance Analysis of INTeractome software. *J Proteomics* 100: 37-43
1014 Tollenaere MAX, Villumsen BH, Blasius M, Nielsen JC, Wagner SA, Bartek J, Beli P, Mailand N, Bekker-
1015 Jensen S (2015) p38- and MK2-dependent signalling promotes stress-induced centriolar
1016 satellite remodelling via 14-3-3-dependent sequestration of CEP131/AZI1. *Nature*
1017 *communications* 6: 10075
1018 Treier M, Staszewski LM, Bohmann D (1994) Ubiquitin-dependent c-Jun degradation in vivo is
1019 mediated by the delta domain. *Cell* 78: 787-798
1020 Tyanova S, Temu T, Sinitcyn P, Carlson A, Hein MY, Geiger T, Mann M, Cox J (2016) The Perseus
1021 computational platform for comprehensive analysis of (prote)omics data. *Nature methods*
1022 13: 731-740
1023 Vides EG, Adhikari A, Chiang CY, Lis P, Purlyte E, Limouse C, Shumate JL, Spinola-Lasso E, Dhekne HS,
1024 Alessi DR *et al* (2022) A feed-forward pathway drives LRRK2 kinase membrane recruitment
1025 and activation. *Elife* 11
1026 Waschbusch D, Michels H, Strassheim S, Ossendorf E, Kessler D, Gloeckner CJ, Barnekow A (2014)
1027 LRRK2 transport is regulated by its novel interacting partner Rab32. *PloS one* 9: e111632
1028 Wauters L, Versees W, Kortholt A (2019) Roco Proteins: GTPases with a Baroque Structure and
1029 Mechanism. *Int J Mol Sci* 20
1030 Wilhelm LP, Zapata-Munoz J, Villarejo-Zori B, Pellegrin S, Freire CM, Toye AM, Boya P, Ganley IG
1031 (2022) BNIP3L/NIX regulates both mitophagy and pexophagy. *The EMBO journal* 41:
1032 e111115
1033 Xue J, Zhang J, Zhang J, Liu J, Wang F, Li K, Liu C (2023) The Parkinson's disease-associated mutation
1034 LRRK2 G2385R alters mitochondrial biogenesis via the PGC-1alpha-TFAM pathway.
1035 *Mitochondrion* 73: 10-18

1036 Yang Y, Ran J, Liu M, Li D, Li Y, Shi X, Meng D, Pan J, Ou G, Aneja R *et al* (2014) CYLD mediates
1037 ciliogenesis in multiple organs by deubiquitinating Cep70 and inactivating HDAC6. *Cell Res*
1038 24: 1342-1353
1039 Yu M, Arshad M, Wang W, Zhao D, Xu L, Zhou L (2018) LRRK2 mediated Rab8a phosphorylation
1040 promotes lipid storage. *Lipids Health Dis* 17: 34
1041 Zhao Y, Bracher-Smith M, Li Y, Harvey K, Escott-Price V, Lewis PA, Manzoni C (2024) Transcriptomics
1042 and weighted protein network analyses of the LRRK2 protein interactome reveal distinct
1043 molecular signatures for sporadic and LRRK2 Parkinson's Disease. *NPJ Parkinsons Dis* 10: 144
1044 Zhao Y, Vavouraki N, Lovering RC, Escott-Price V, Harvey K, Lewis PA, Manzoni C (2023) Tissue
1045 specific LRRK2 interactomes reveal a distinct striatal functional unit. *PLoS Comput Biol* 19:
1046 e1010847
1047 Zheng L, Bernard-Marissal N, Moullan N, D'Amico D, Auwerx J, Moore DJ, Knott G, Aebischer P,
1048 Schneider BL (2017) Parkin functionally interacts with PGC-1α to preserve mitochondria and
1049 protect dopaminergic neurons. *Human molecular genetics* 26: 582-598
1050 Zhu H, Hixson P, Ma W, Sun J (2024) Pharmacology of LRRK2 with type I and II kinase inhibitors
1051 revealed by cryo-EM. *Cell Discov* 10: 10
1052 Zhu H, Tonelli F, Turk M, Prescott A, Alessi DR, Sun J (2023) Rab29-dependent asymmetrical
1053 activation of leucine-rich repeat kinase 2. *Science* 382: 1404-1411
1054 Zimprich A, Biskup S, Leitner P, Lichtner P, Farrer M, Lincoln S, Kachergus J, Hulihan M, Uitti RJ, Calne
1055 DB *et al* (2004) Mutations in LRRK2 cause autosomal-dominant parkinsonism with
1056 pleomorphic pathology. *Neuron* 44: 601-607

1057 **Tables:**

Accession	Gene name	Protein name	Jaccard score
Q5S007	LRRK2	Leucine-rich repeat serine/threonine-protein kinase 2 (bait)	1.000000
Q9NQC7	**CYLD**	**Ubiquitin carboxyl-terminal hydrolase CYLD**	**0.848485**
Q6P2H3	CEP85	Centrosomal protein of 85 kDa	0.846626
Q96JH7	VCPIP1	Deubiquitinating protein VCPIP1	0.834286
Q96L93	KIF16B	Kinesin-like protein KIF16B	0.832335
P78312	FAM193A	Protein FAM193A	0.817647
Q8NEY1	NAV1	Neuron navigator 1	0.817073
Q7Z2T5	TRMT1L	TRMT1-like protein	0.815951
Q5SZL2	CEP85L	Centrosomal protein of 85 kDa-like	0.810127
O95684	CEP43	Centrosomal protein 43	0.809816
Q96RS0	TGS1	Trimethylguanosine synthase	0.798742

1058

1059 **Table 1:** 10 IDs with the highest Jaccard score underlying identified “Cluster 2”. The DUB CYLD (bold)
1060 shows highest co-evolution to LRRK2.

Accession	Protein name	Gene name	P-value	Log2 T-test difference
P81605	Dermcidin	DCD	2.91844	3.3
Q9UPN4	Centrosomal protein of 131 kDa	CEP131	4.15494	2.2
Q49A88	Coiled-coil domain-containing protein 14	CCDC14	5.39373	2.1
Q9Y2D8	Afadin- and alpha-actinin-binding protein	SSX2IP	2.98866	2.1
O75665	Oral-facial-digital syndrome 1 protein	OFD1	7.92350	2.0
Q15154	Pericentriolar material 1 protein	PCM1	6.62987	1.8
Q9UHB6	LIM domain and actin-binding protein 1	LIMA1	2.96451	1.7
Q8WXW3	Progesterone-induced-blocking factor 1	PIBF1	4.62801	1.5
Q6WCQ1	Myosin phosphatase Rho-interacting protein	MPRIP	7.40967	1.5
Q14596	Next to BRCA1 gene 1 protein	NBR1	3.34347	1.3
Q5TB80	Centrosomal protein of 162 kDa	CEP162	3.46643	1.3
Q8WWI1	LIM domain only protein 7	LMO7	5.84664	1.3

1061

1062 **Table 2:** Enriched proteins in the LRRK2 proximity proteome upon MLi-2 treatment (FDR-controlled
1063 T-test).

Accession	Protein name	Gene name	P-value (-log10)	Log2 T-test difference
O14966	Ras-related protein Rab-7L1	RAB29	9,72545	10,5
Q8IZA0	Dyslexia-associated protein KIAA0319-like protein	KIAA0319L	5,00209	4,9
Q6WKZ4	Rab11 family-interacting protein 1	RAB11FIP1	4,56815	4,6
O15126	Secretory carrier-associated membrane protein 1	SCAMP1	4,09385	3,5
Q9UIQ6	Leucyl-cystinyl aminopeptidase;Leucyl-cystinyl aminopeptidase, pregnancy serum form	LNPEP	4,33552	3,4
Q9H2J7	Sodium-dependent neutral amino acid transporter B(0)AT2	SLC6A15	5,06972	2,9
Q96QD8	Sodium-coupled neutral amino acid transporter 2	SLC38A2	2,89271	2,9
Q13586	Stromal interaction molecule 1	STIM1	3,12115	2,8
P98194	Calcium-transporting ATPase type 2C member 1	ATP2C1	5,00347	2,6
Q9H2H9	Sodium-coupled neutral amino acid transporter 1	SLC38A1	2,37723	2,6
O75976	Carboxypeptidase D	CPD	3,20952	2,6
Q14126	Desmoglein-2	DSG2	4,31421	2,5
P51809	Vesicle-associated membrane protein 7	VAMP7	4,02209	2,5
Q8NDI1	EH domain-binding protein 1	EHBP1	2,37346	2,5
Q8TBA6	Golgin subfamily A member 5	GOLGA5	3,0259	2,4
Q9BXF6	Rab11 family-interacting protein 5	RAB11FIP5	2,9101	2,4
Q7L804	Rab11 family-interacting protein 2	RAB11FIP2	3,33154	2,2
Q6IAA8	Ragulator complex protein LAMTOR1	LAMTOR1	3,23604	2,1
P61006	Ras-related protein Rab-8A	RAB8A	3,56486	2,1
P11717	Cation-independent mannose-6-phosphate receptor	IGF2R	5,71543	2,0
Q13190	Syntaxin-5	STX5	3,88884	2,0
Q15836;P63027	Vesicle-associated membrane protein 3;Vesicle-associated membrane protein 2	VAMP3;VAMP2	3,67019	2,0
Q92692	Nectin-2	PVRL2	3,06334	2,0
Q6NXT4	Zinc transporter 6	SLC30A6	3,47208	1,8
Q96A65	Exocyst complex component 4	EXOC4	2,51947	1,7
Q14141	Septin-6	Sept6	3,87782	1,7
Q04656	Copper-transporting ATPase 1	ATP7A	2,77415	1,7
Q7Z2W4	Zinc finger CCCH-type antiviral protein 1	ZC3HAV1	2,62567	1,6
P78310	Coxsackievirus and adenovirus receptor	CXADR	2,87956	1,4
P08195	4F2 cell-surface antigen heavy chain	SLC3A2	2,43497	1,4
P02786	Transferrin receptor protein 1;Transferrin receptor protein 1, serum form	TFRC	3,21618	1,3
Q07960	Rho GTPase-activating protein 1	ARHGAP1	2,65929	1,3
O60271	C-Jun-amino-terminal kinase-interacting protein 4	SPAG9	3,80826	1,3
P42167	Lamina-associated polypeptide 2, isoforms beta/gamma;Thymopoietin;Thymopentin	TMPO	3,54449	1,2
Q9BSJ8	Extended synaptotagmin-1	ESYT1	3,59064	1,0
Q14739	Lamin-B receptor	LBR	3,12029	0,8

Table 3: Enriched proteins in the RAB29-dependent LRRK2 proximity proteome (FDR-controlled T-test).

1067 **Figure legends**

1068 **Figure 1:** (A) Workflow of the BioID analysis and post processing of the data. (B) Overlap between
1069 the different BioID approaches. Enriched proteins were determined by relative label-free
1070 quantification (combined with an FDR-controlled T-test, P = 0.05) of BioID LRRK2 vs the
1071 corresponding tag-only control: BioID1-LRRK2/BioID1-tag: N = 8, BioID2-LRRK2/BioID2: N = 9,
1072 miniTurbo-LRRK2/miniTurbo tag: N = 8.

1073

1074 **Figure 2:** LRRK2 interactome functional enrichment. A) the LRRK2 BioID interaction network was
1075 mapped on known PPIs from IntAct via Cytoscape. The edges' color and thickness for mapped
1076 interactions are proportional to IntAct MI score, else they are colored in gray with constant
1077 thickness. Modules within the network have been identified through the Glay method of the
1078 Autoannotate app and nodes colored accordingly. Labels were calculated using the 'Adjacent Words'
1079 setting of the WordCloud algorithm, based on significantly enriched (FDR < 0.01) Gene Ontology
1080 (GO) Biological Processes and Cellular Component terms associated with each gene in the network ;
1081 B) Venn diagram showing the overlap between the BioID interaction sets and known LRRK2
1082 interactions in IntAct; barplots showing the top 15 most significant terms obtained through String's
1083 functional enrichment of C) Compartments, D) GO Biological Process and D) Interpro domains.

1084

1085 **Figure 3:** Co-evolution analysis of LRRK2 interactome. (A) Distribution of co-evolution metric (i.e.
1086 Jaccard score) among the different LRRK2 interaction sets, including IntAct interaction types and
1087 BIOID. P-values have been computed with a two-sided Mann-Whitney test with Bonferroni
1088 correction (* $P < 0.05$, ** $P < 0.01$, *** $P < 0.001$, **** $P < 0.0001$). The plot shows the
1089 comparison between 2062 independent samples divided in 5 classes with the following
1090 number of elements: association 1424, physical 68, direct 215, non-enzymatic direct 166,
1091 BioID 189. P-values: association-direct: 1.2E-11; association-non-enzymatic direct: 5.8E-19;
1092 association-BioID: 6.1E-29; physical-non-enzymatic direct: 0.0017; physical-BioID: 2.7E-5;
1093 direct-BioID: 0.0082. Violin plots show the median as the white central dot and first and
1094 third quartiles as bounds of the thicker black line (box); the whiskers extend to the last data
1095 point within 1.5 times the interquartile range (IQR) from the box's boundaries. (B)
1096 predictiveness of LRRK2 interaction type via co-evolution (C) Heatmap showing the hierarchical
1097 clustering based on the degree of co-evolution (Jaccard score) of the LRRK2 proximity proteome. (D)
1098 String network of the proteins most co-evolved with LRRK2 participating to cluster 2. Nodes are

1099 colored in gray or light-gray according to modules membership determined with the MCL approach
1100 available from the Cytoscape clusterMaker app. Node rims are colored according to enriched
1101 processes. (E) Dot plot showing top 15 significantly enriched (FDR < 0.01) categories from the string
1102 network of cluster 2. Values on the x axis display the ratio of genes of the term participating to the
1103 network over the total number of genes in that category. The ratio of the dot is proportional to the
1104 number of genes of that category in the network, while the node color is the darker the more
1105 significant is the category enrichment. Only categories with at least 5 genes have been displayed.
1106 Representative, enriched categories have been colored with the same color scheme as in panel (D).
1107 (F) Validation of CYLD as part of the LRRK2 proximity proteome by Western blot. Because suitable
1108 antibodies for detecting CYLD at endogenous levels were not available, a FLAG-HA–tagged CYLD
1109 construct was recombinantly expressed for this experiment. This contrasts with the MS–based
1110 approach, which relied on endogenous protein levels. Prior to antibody incubation, the membrane
1111 was horizontally cut above the 140 kDa marker (expected molecular weight of CYLD: ~110 kDa). The
1112 upper part of the blot was probed with an anti-LRRK2 antibody (24D8), while the lower part was
1113 probed with anti-FLAG and subsequently re-probed with anti-CYLD antibodies. (G) Effect of CYLD co-
1114 expression on steady-state LRRK2 levels: LRRK2 WT or Y1699C was co-expressed with CYLD or empty
1115 vector control. LRRK2 protein levels were normalized by β-actin. Statistical significance was assessed
1116 using unpaired two-tailed t-tests (P-values: A-B: 0.0951; C-D: 4.5E-8; N = 6 biological replicates; error
1117 bars = SD) (left panel). Reconstructed Capillary Western signals and confirmation of CYLD expression
1118 by Western blot. On the capillary Western blot, LRRK2 migrates at a lower molecular weight (right
1119 panel).

1120

1121 **Figure 4:** 3D complexes prediction and analysis of LRRK2 interactome (A) workflow of the structural
1122 bioinformatics analysis of LRRK2 interactome; (B) on the left the heatmap showing the hierarchical
1123 clustering based on pairwise RMSD calculation of LRRK2's chain in the different complexes. On the
1124 right two representative conformations of LRRK2 in the "locked" and "unlocked" conformation to
1125 mark the two main clusters; (C) cartoon representation of "locked" (tomato) and "unlocked" (light
1126 green) superimposed LRRK2 conformations; (D) violin plot of the distribution of RMSD calculated
1127 with respect to the reference LRRK2 experimental structure (PDB 7LHW) for the locked and unlocked
1128 clusters (P = 3.8E-20; comparison between 48 locked and 148 unlocked independent samples). Color
1129 scheme as in (C); (E) distribution of the Jaccard score for the locked and unlocked clusters (P =
1130 0.0013; comparison between 48 locked and 148 unlocked independent samples). Color scheme as in
1131 (C). P-values for violin plots in D and E have been computed with a two-sided Mann-Whitney
1132 test (* $P < 0.05$, ** $P < 0.01$, *** $P < 0.001$, **** $P < 0.0001$). Violin plots show the median as

1133 the white central dot and first and third quartiles as bounds of the thicker black line (box);
1134 the whiskers extend to the last data point within 1.5 times the interquartile range (IQR)
1135 from the box's boundaries; (F) Venn diagram of the enriched terms in the locked and unlocked
1136 clusters. Color scheme as in (C); (G) Top 10 exclusively enriched (FDR < 0.01) terms in the locked and
1137 unlocked clusters.

1138

1139 **Figure 5:** Interface analysis of LRRK2's 3D interactome (A) interface fingerprint of the LRRK2
1140 complexes via distogram calculation. Cells contain the minimum expected distance obtained from
1141 the distograms of any residue of each interactor (row) to every residue in LRRK2 (column). Rows are
1142 color annotated based on confidence score, Jaccard and RMSD from reference LRRK2 structure
1143 (PDB: 7LHW); (B) representative structure of the Core cluster (i.e. LRRK2-ANAPC5 complex); (C)
1144 representative structures of the WD40 cluster; (D) representative structures of the ARM binding
1145 mode cluster (i.e. LRRK2- DCUN1D4 complex); distribution among different interface cluster of the
1146 (E) confidence score, (F) RMSD and (G) Jaccard score descriptors. (C), (D) and (E) show the
1147 comparison between 196 independent samples divided in 4 cluster with the following
1148 number of elements: 50 Core, 26 WD40, 11 ARM and 109 Other. P-values have been
1149 computed with a two-sided Mann-Whitney test with Bonferroni correction (* $P < 0.05$, **
1150 $P < 0.01$, *** $P < 0.001$, **** $P < 0.0001$). Violin plots show the median as the white central
1151 dot and first and third quartiles as bounds of the thicker black line (box); the whiskers
1152 extend to the last data point within 1.5 times the interquartile range (IQR) from the box's
1153 boundaries. (C) P-values: Core-WD40: 1.1E-8; Core-ARM: 1.0; Core-Other: 4.9E-14; WD40-
1154 ARM: 0.0035; WD40-Other: 1.0; ARM-Other: 0.0030. (D) P-values: Core-WD40: 0.0040;
1155 Core-ARM: 1.0; Core-Other: 1.0; WD40-ARM: 1.0; WD40-Other: 5.6E-4; ARM-Other: 1.0. (E)
1156 P-values: Core-WD40: 0.099; Core-ARM: 1.0; Core-Other: 1.0; WD40-ARM: 1.0; WD40-
1157 Other: 0.0026; ARM-Other: 1.0.

1158

1159 **Figure 6:** Different effects of type I and type II inhibitors and RAB29 on the LRRK2 proximity
1160 proteome. (A) Volcano plot MLi-2 vs DMSO (moderated permutation-based T-test, FDR = 0.05; S0 =
1161 0.1, N = 7). (B) Stringified network of the MLi-2 interactome from (A) mapped to IntAct known
1162 interactions. Edges' color and thickness for mapped interactions are proportional to IntAct MI score,
1163 else they are colored in gray with constant thickness. Node rims are colored according to enriched
1164 processes; (C) Dot plot showing top 15 significantly enriched (FDR < 0.01) categories from the LRRK2-

1165 MLi-2 interactome. Values on the x axis display the ratio of genes of the term participating to the
1166 network over the total number of genes in that category. The ratio of the dot is proportional to the
1167 number of genes of that category in the network, while the node color is the darker the more
1168 significant is the category enrichment. Only categories with at least 5 genes have been displayed.
1169 Representative, enriched categories have been colored with the same color scheme as in panel C.
1170 (D) Scheme highlighting the function of centriolar satellites and the core protein PCM1 in ciliation
1171 (Hori & Toda, 2017, modified) (E) BioID analysis following PCM1 knockdown and MLi-2 treatment.
1172 Shown are eluates obtained after streptavidin-based enrichment of biotinylated proteins. (F) Violin
1173 plot reporting the Jaccard Score distribution in different data sets. P-values have been computed
1174 with a two-sided Mann-Whitney test with Bonferroni correction (* $P < 0.05$; P = 0.0499 for T-
1175 test BioID vs MLi-2 BioID; comparison between 188 BioID, 431 T-test BioID, 36 RAB29 BioID
1176 and 9 MLi-2 BioID independent samples; only P-values < 0.05 are shown). Violin plots show
1177 the median as the white central dot and first and third quartiles as bounds of the thicker
1178 black line (box); the whiskers extend to the last data point within 1.5 times the interquartile
1179 range (IQR) from the box's boundaries; (G) Volcano-plot (+/-RAB29): mT-LRRK2 proximity
1180 proteome following RAB29 co-expression (moderated FDR-based T-test, P = 0.05; S0 = 0.1, N = 9).
1181 RAB29 redirects LRRK2 to lysosomal PPI networks; (H) Stringified network of the RAB29 over-
1182 expression interactome from (G) mapped to IntAct known interactions. Edges' color and thickness
1183 for mapped interactions are proportional to IntAct MI score, else they are colored in gray with
1184 constant thickness. Node rims are colored according to enriched processes; (I) Dot plot showing top
1185 15 significantly enriched (FDR < 0.01) categories from the LRRK2-RAB29 over-expression
1186 interactome. Values on the x axis display the ratio of genes of the term participating to the network
1187 over the total number of genes in that category. The ratio of the dot is proportional to the number
1188 of genes of that category in the network, while the node color is the darker the more significant is
1189 the category enrichment. Only categories with at least 5 genes have been displayed. Representative,
1190 enriched categories have been colored with the same color scheme as in panel H.

1191 **Figure 7:** AF-structural modeling of MLi-2 and Rab29 interactomes. (A) Hierarchical clustering of
1192 pairwise RMSD of LRRK2 chain in the different complexes; B) LRRK2-RAB8A predicted complex; (C)
1193 LRRK2-RAB29 predicted complex; (D) violin plot of the distribution of RMSD calculated with respect
1194 to the reference LRRK2 experimental structure (PDB 7LHW) for the locked and unlocked clusters.
1195 Color scheme as in 4C (P = 3.8E-6; comparison between 14 locked and 32 unlocked independent
1196 samples); (E) distribution of the Jaccard score for the locked and unlocked clusters (P = 0.14;
1197 comparison between 14 locked and 32 unlocked independent samples). Color scheme as in 4C. P-

1198 values in violin plots in (D) and (E) have been computed with a two-sided Mann-Whitney
1199 test (* $P < 0.05$, ** $P < 0.01$, *** $P < 0.001$, **** $P < 0.0001$). Violin plots show the median as
1200 the white central dot and first and third quartiles as bounds of the thicker black line (box);
1201 the whiskers extend to the last data point within 1.5 times the interquartile range (IQR)
1202 from the box's boundaries; (F) Venn diagram of the enriched terms in the locked and unlocked
1203 clusters. Color scheme as in 4C; (G) Top exclusively enriched (FDR < 0.01) terms in the locked and
1204 unlocked clusters. Color scheme as in 4C.

1205

1206 **Figure EV1:** (A) interaction fingerprint clustering of LRRK2's modulators (MLi-2 and RAB29)
1207 interactomes. Cells contain the minimum expected distance obtained from the distograms of any
1208 residue of each interactor (row) to every residue in LRRK2 (column). Rows are color annotated based
1209 on confidence score, Jaccard, RMSD from reference LRRK2 structure (PDB: 7LHW) and experiment
1210 type (either MLi-2 or RAB29 over-expression); (B) interaction fingerprint of LRRK2 and interacting
1211 RABs (from IntAct).

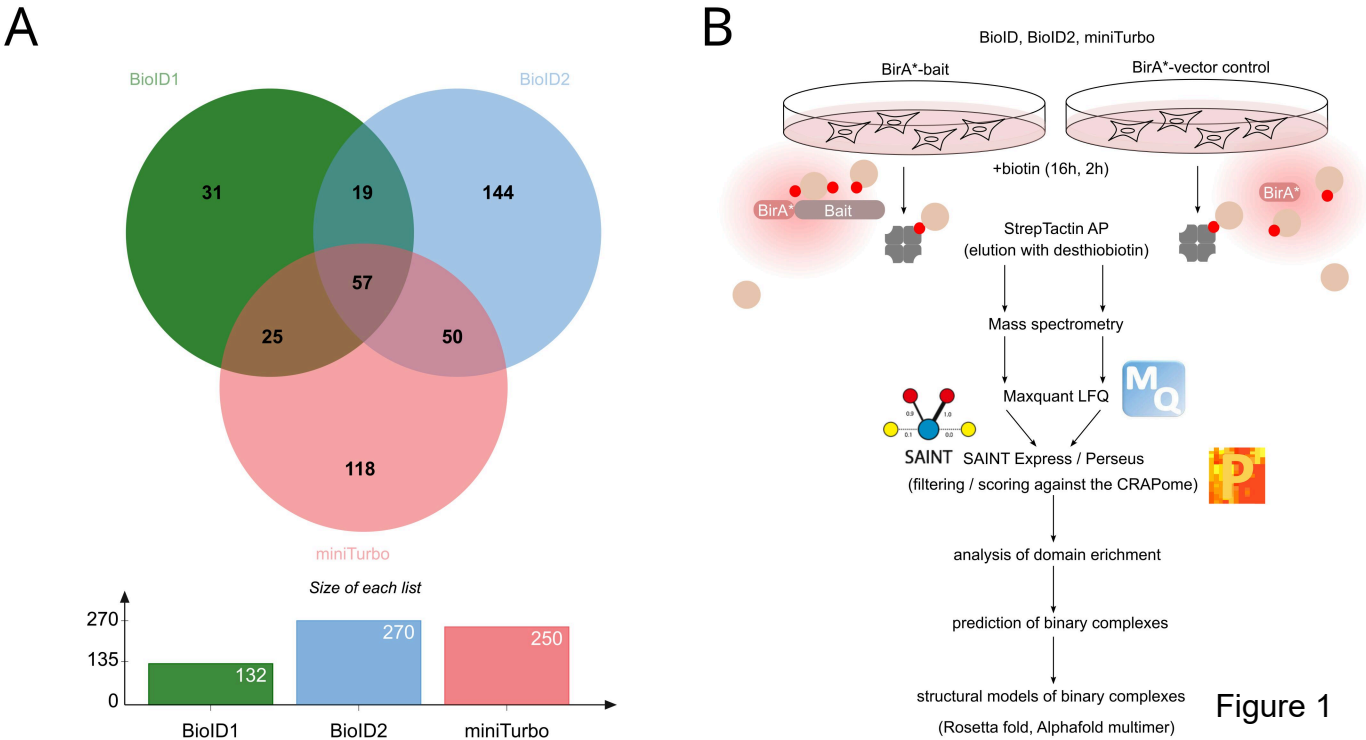
A
BioID1
BioID2
miniTurbo
31
19
144
57
25
50
118
Size of each list
270
135
0
132
270
250
BioID1
BioID2
miniTurbo
B
BioID, BioID2, miniTurbo
BirA*-bait
BirA*-vector control
+biotin (16h, 2h)
BirA*
Bait
BirA*
StrepTactin AP
(elution with desthiobiotin)
Mass spectrometry
Maxquant LFQ
SAINT
SAINT Express / Perseus
(filtering / scoring against the CRAPome)
analysis of domain erichment
prediction of binary complexes
structural models of binary complexes
(Rosetta fold, Alphafold multimer)

Figure 1

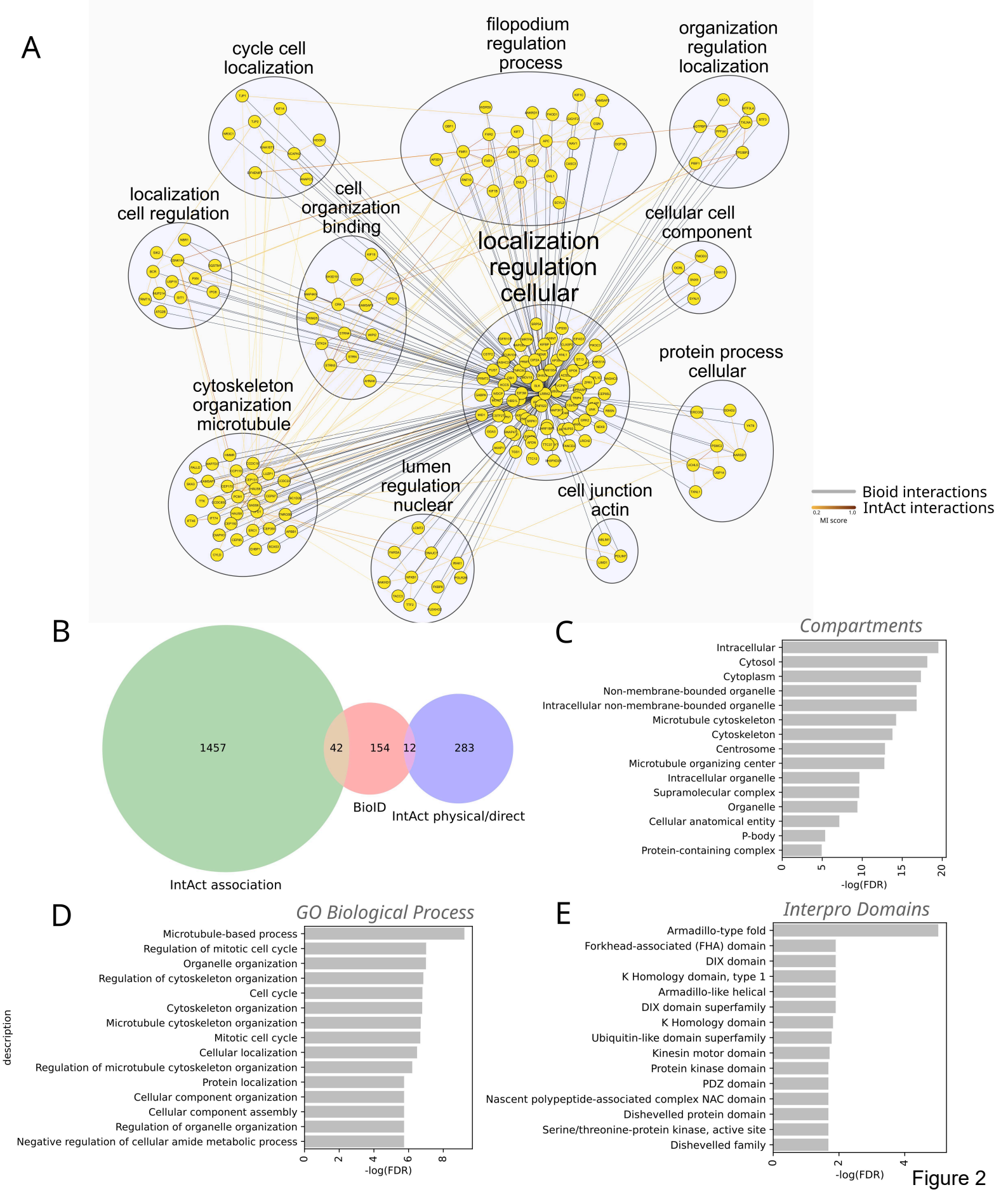
A
cycle cell localization
filopodium regulation process
organization regulation localization
localization cell regulation
cell organization binding
localization regulation cellular
cellular cell component
protein process cellular
cytoskeleton organization microtubule
lumen regulation nuclear
cell junction actin
Bioid interactions
IntAct interactions
0.2
1.0
MI score
B
1457
42
154
12
283
BioID
IntAct physical/direct
IntAct association
C
Compartments
Intracellular
Cytosol
Cytoplasm
Non-membrane-bounded organelle
Intracellular non-membrane-bounded organelle
Microtubule cytoskeleton
Cytoskeleton
Centrosome
Microtubule organizing center
Intracellular organelle
Supramolecular complex
Organelle
Cellular anatomical entity
P-body
Protein-containing complex
0
5
10
15
20
-log(FDR)
D
GO Biological Process
description
Microtubule-based process
Regulation of mitotic cell cycle
Organelle organization
Regulation of cytoskeleton organization
Cell cycle
Cytoskeleton organization
Microtubule cytoskeleton organization
Mitotic cell cycle
Cellular localization
Regulation of microtubule cytoskeleton organization
Protein localization
Cellular component organization
Cellular component assembly
Regulation of organelle organization
Negative regulation of cellular amide metabolic process
0
2
4
6
8
-log(FDR)
E
Interpro Domains
Armadillo-type fold
Forkhead-associated (FHA) domain
DIX domain
K Homology domain, type 1
Armadillo-like helical
DIX domain superfamily
K Homology domain
Ubiquitin-like domain superfamily
Kinesin motor domain
Protein kinase domain
PDZ domain
Nascent polypeptide-associated complex NAC domain
Dishevelled protein domain
Serine/threonine-protein kinase, active site
Dishevelled family
0
2
4
-log(FDR)

Figure 2

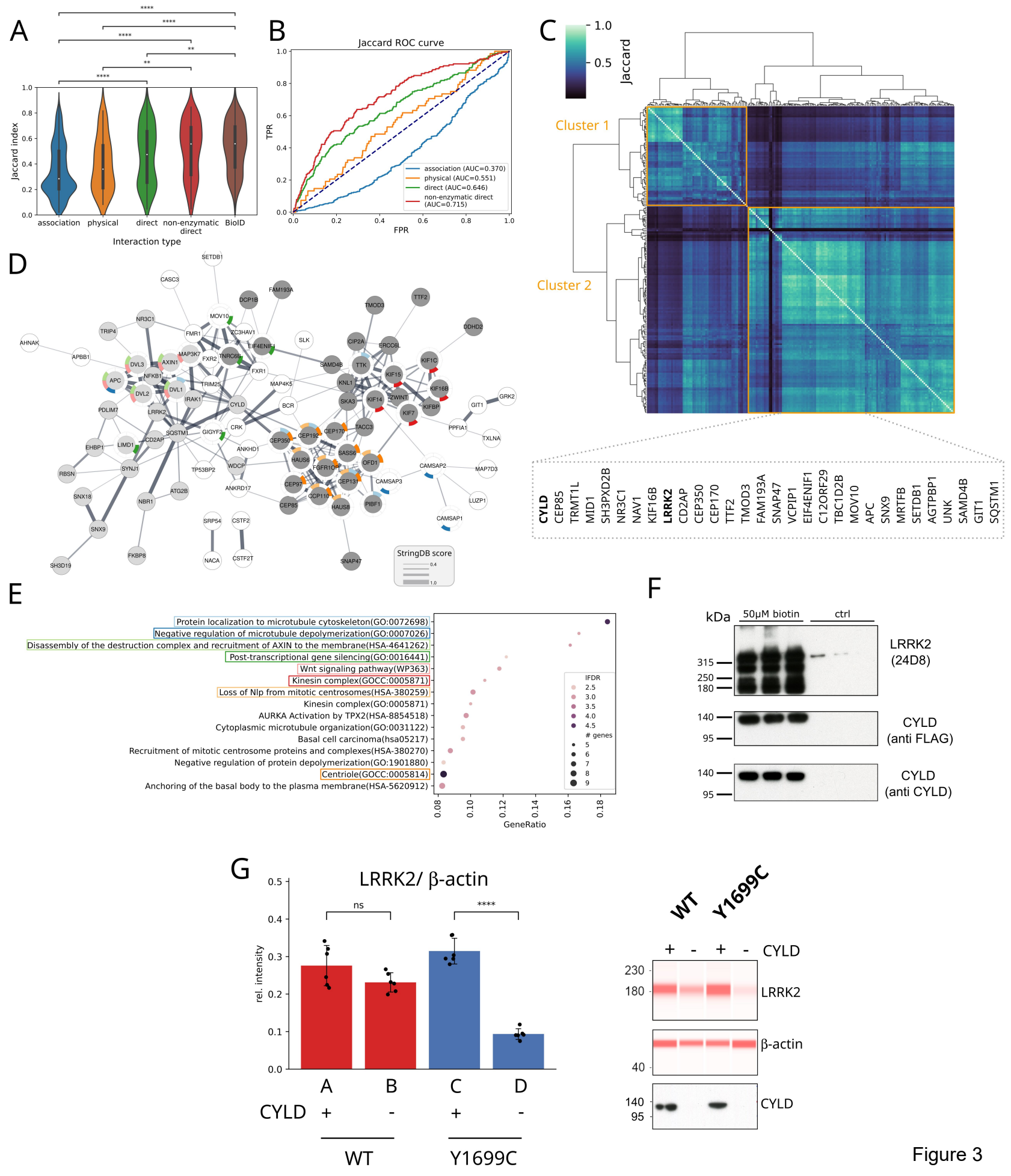
A
Jaccard index
association
physical
direct
non-enzymatic direct
BioID
Interaction type
B
Jaccard ROC curve
TPR
FPR
association (AUC=0.370)
physical (AUC=0.551)
direct (AUC=0.646)
non-enzymatic direct (AUC=0.715)
C
Jaccard
Cluster 1
Cluster 2
CYLD
CEP85
TRMT1L
MID1
SH3PXD2B
NR3C1
NAV1
KIF16B
LRRK2
CD2AP
CEP350
CEP170
TTF2
TMOD3
FAM193A
SNAP47
VCPIP1
EIF4ENIF1
C12ORF29
TBC1D2B
MOV10
APC
SNX9
MRTFB
SETDB1
AGTPBP1
UNK
SAMD4B
GIT1
SQSTM1
D
StringDB score
E
Protein localization to microtubule cytoskeleton(GO:0072698)
Negative regulation of microtubule depolymerization(GO:0007026)
Disassembly of the destruction complex and recruitment of AXIN to the membrane(HSA-4641262)
Post-transcriptional gene silencing(GO:0016441)
Wnt signaling pathway(WP363)
Kinesin complex(GOCC:0005871)
Loss of Nlp from mitotic centrosomes(HSA-380259)
Kinesin complex(GO:0005871)
AURKA Activation by TPX2(HSA-8854518)
Cytoplasmic microtubule organization(GO:0031122)
Basal cell carcinoma(hsa05217)
Recruitment of mitotic centrosome proteins and complexes(HSA-380270)
Negative regulation of protein depolymerization(GO:1901880)
Centriole(GOCC:0005814)
Anchoring of the basal body to the plasma membrane(HSA-5620912)
IFDR
genes
GeneRatio
F
kDa
50μM biotin
ctrl
LRRK2 (24D8)
CYLD (anti FLAG)
CYLD (anti CYLD)
G
LRRK2/ β-actin
rel. intensity
ns
****
A
B
C
D
CYLD
WT
Y1699C
β-actin

Figure 3

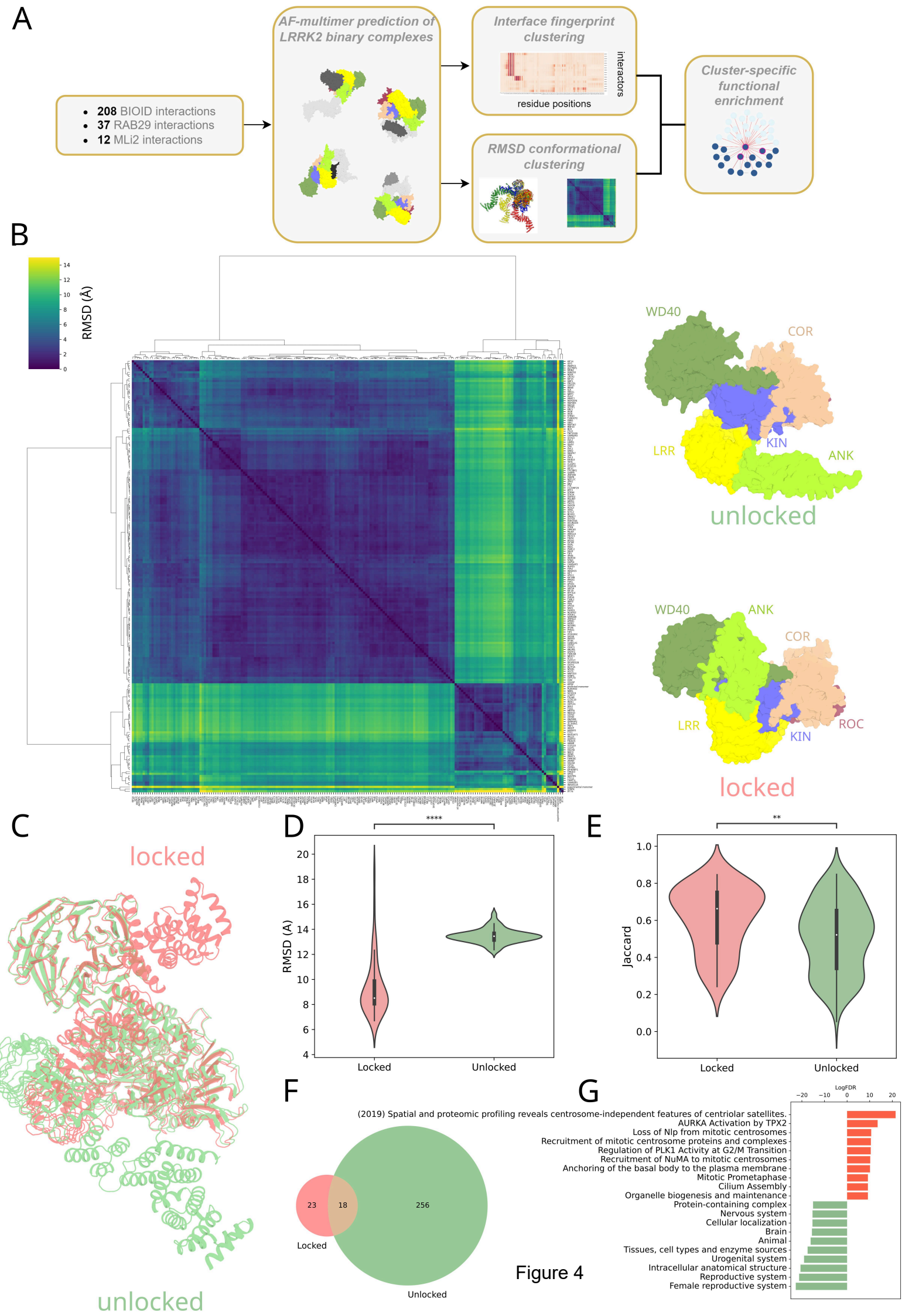
A
208 BIOID interactions
37 RAB29 interactions
12 MLi2 interactions
AF-multimer prediction of LRRK2 binary complexes
Interface fingerprint clustering
interactors
residue positions
RMSD conformational clustering
Cluster-specific functional enrichment
B
RMSD (Å)
WD40
COR
LRR
KIN
ANK
unlocked
WD40
ANK
COR
LRR
ROC
KIN
locked
C
locked
unlocked
D
****
RMSD (A)
Locked
Unlocked
E
**
Jaccard
Locked
Unlocked
F
23
18
256
Locked
Unlocked
G
LogFDR
(2019) Spatial and proteomic profiling reveals centrosome-independent features of centriolar satellites.
AURKA Activation by TPX2
Loss of Nlp from mitotic centrosomes
Recruitment of mitotic centrosome proteins and complexes
Regulation of PLK1 Activity at G2/M Transition
Recruitment of NuMA to mitotic centrosomes
Anchoring of the basal body to the plasma membrane
Mitotic Prometaphase
Cilium Assembly
Organelle biogenesis and maintenance
Protein-containing complex
Nervous system
Cellular localization
Brain
Animal
Tissues, cell types and enzyme sources
Urogenital system
Intracellular anatomical structure
Reproductive system
Female reproductive system

Figure 4

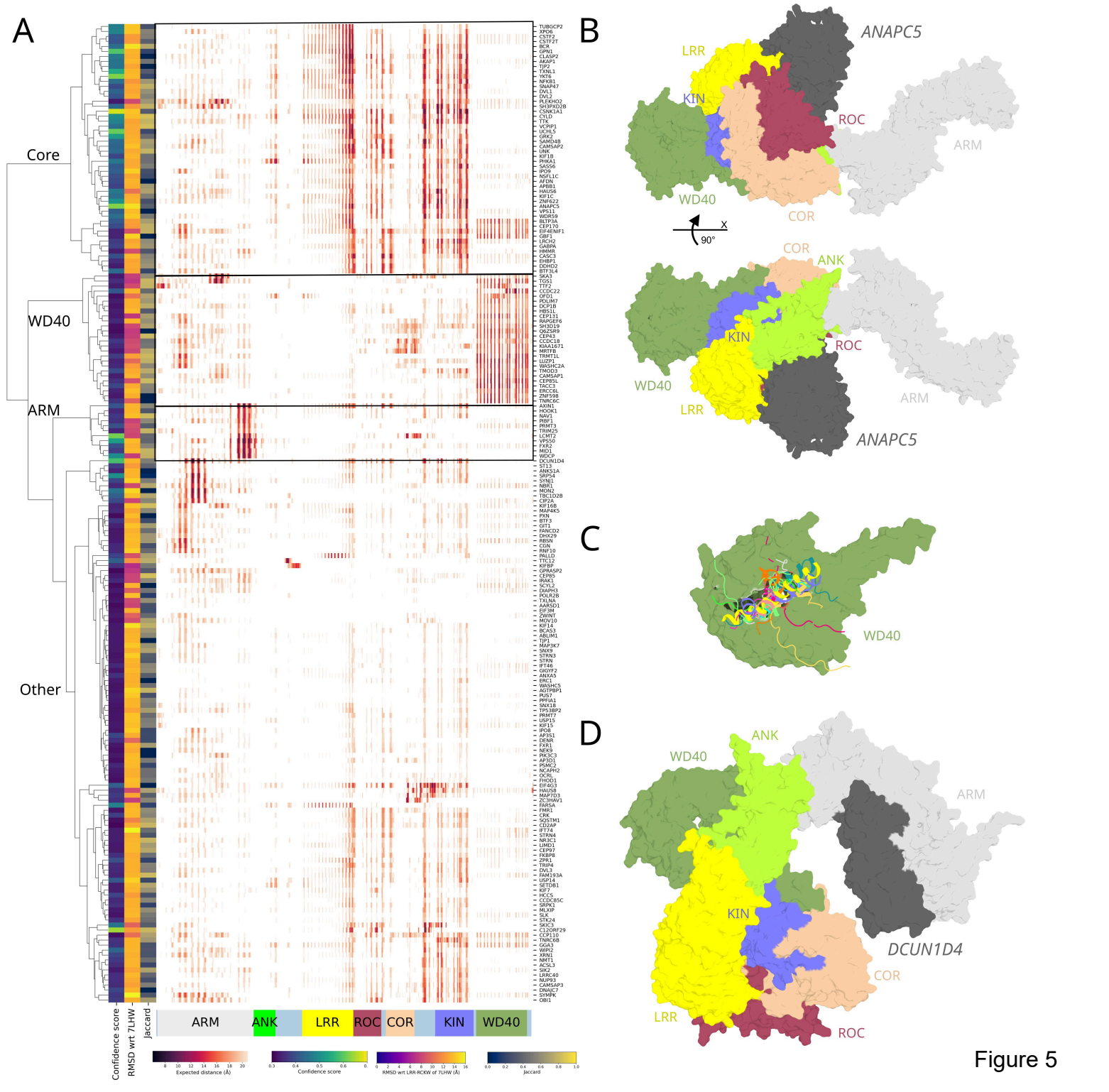
A
Core
WD40
ARM
Other
Confidence score
RMSD wrt 7LHW
Jaccard
ARM
ANK
LRR
ROC
COR
KIN
WD40
Expected distance (Å)
Confidence score
RMSD wrt LRR-RCKW of 7LHW (Å)
Jaccard
B
ANAPC5
LRR
KIN
ROC
ARM
WD40
COR
x
90°
COR
ANK
KIN
ROC
WD40
ARM
LRR
ANAPC5
C
WD40
D
ANK
WD40
ARM
KIN
DCUN1D4
COR
LRR
ROC

Figure 5

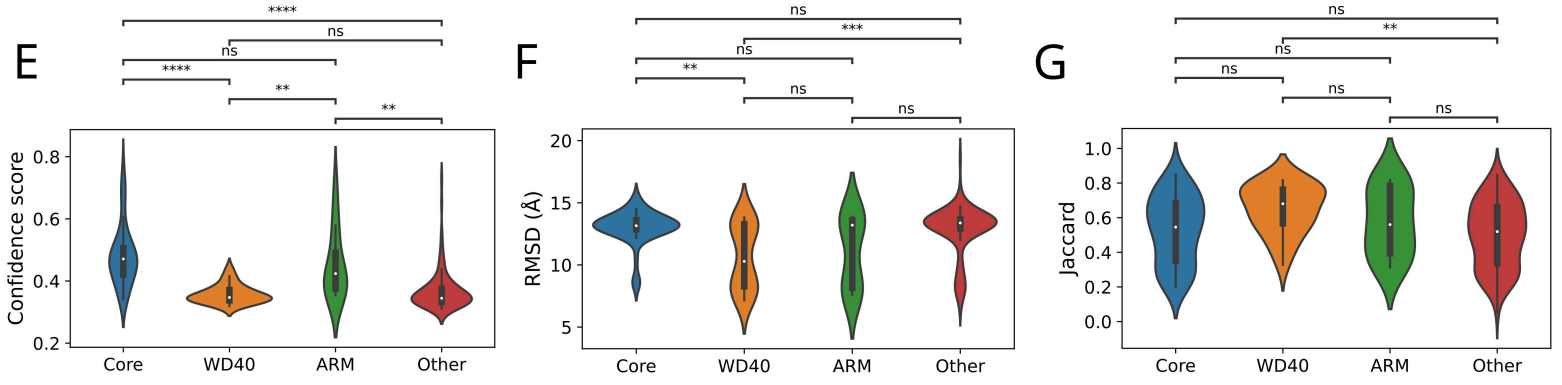
E
****
ns
ns
****
**
**
Confidence score
0.2
0.4
0.6
0.8
Core
WD40
ARM
Other
F
ns
***
ns
**
ns
ns
RMSD (Å)
5
10
15
20
Core
WD40
ARM
Other
G
ns
**
ns
ns
ns
ns
Jaccard
0.0
0.2
0.4
0.6
0.8
1.0
Core
WD40
ARM
Other

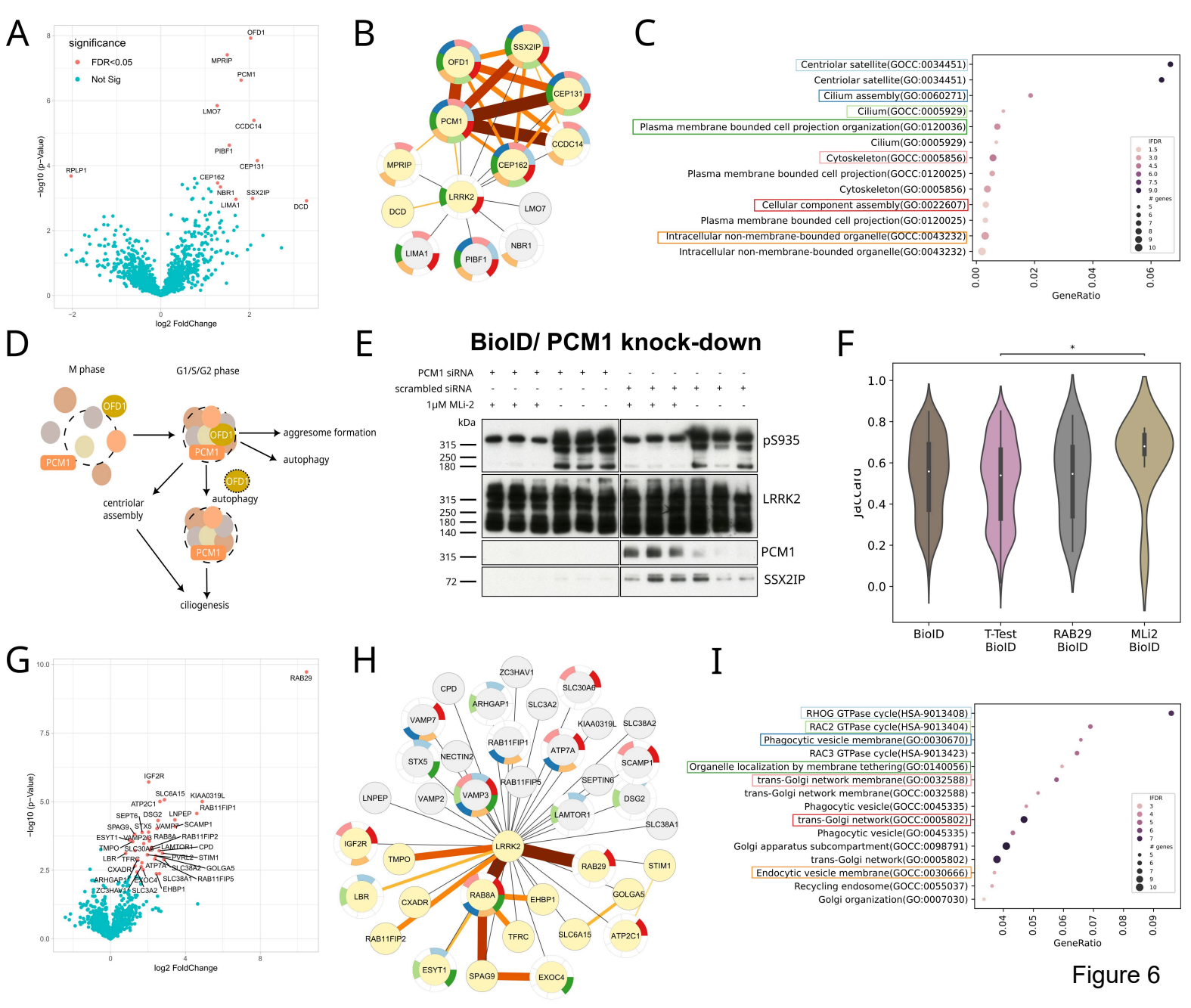
A
significance
FDR<0.05
Not Sig
OFD1
MPRIP
PCM1
LMO7
CCDC14
PIBF1
CEP131
RPLP1
CEP162
NBR1
SSX2IP
LIMA1
DCD
−log10 (p-Value)
log2 FoldChange
B
SSX2IP
OFD1
CEP131
PCM1
CCDC14
MPRIP
CEP162
LRRK2
DCD
LMO7
NBR1
LIMA1
PIBF1
C
Centriolar satellite(GOCC:0034451)
Centriolar satellite(GO:0034451)
Cilium assembly(GO:0060271)
Cilium(GOCC:0005929)
Plasma membrane bounded cell projection organization(GO:0120036)
Cilium(GO:0005929)
Cytoskeleton(GOCC:0005856)
Plasma membrane bounded cell projection(GOCC:0120025)
Cytoskeleton(GO:0005856)
Cellular component assembly(GO:0022607)
Plasma membrane bounded cell projection(GO:0120025)
Intracellular non-membrane-bounded organelle(GOCC:0043232)
Intracellular non-membrane-bounded organelle(GO:0043232)
FDR
genes
GeneRatio
D
M phase
G1/S/G2 phase
OFD1
PCM1
aggresome formation
autophagy
centriolar assembly
ciliogenesis
E
BioID/ PCM1 knock-down
PCM1 siRNA
scrambled siRNA
1μM MLi-2
kDa
pS935
LRRK2
PCM1
SSX2IP
F
BioID
T-Test BioID
RAB29 BioID
MLi2 BioID
G
RAB29
IGF2R
SLC6A15
KIAA0319L
ATP2C1
RAB11FIP1
SEPT6
DSG2
LNPEP
SCAMP1
SPAG9
STX5
VAMP7
ESYT1
VAMP2
RAB8A
RAB11FIP2
TMPO
SLC30A6
LAMTOR1
CPD
LBR
TFRC
PVRL2
STIM1
CXADR
ATP7A
SLC38A2
GOLGA5
ARHGAP1
EXOC4
SLC38A1
RAB11FIP5
ZC3HAV1
SLC3A2
EHBP1
−log10 (p-Value)
log2 FoldChange
H
ZC3HAV1
CPD
SLC30A6
ARHGAP1
SLC3A2
VAMP7
KIAA0319L
SLC38A2
RAB11FIP1
ATP7A
STX5
NECTIN2
SCAMP1
RAB11FIP5
SEPTIN6
LNPEP
VAMP2
VAMP3
DSG2
LAMTOR1
SLC38A1
IGF2R
TMPO
LRRK2
RAB29
STIM1
LBR
CXADR
RAB8A
EHBP1
GOLGA5
RAB11FIP2
TFRC
SLC6A15
ATP2C1
ESYT1
SPAG9
EXOC4
I
RHOG GTPase cycle(HSA-9013408)
RAC2 GTPase cycle(HSA-9013404)
Phagocytic vesicle membrane(GO:0030670)
RAC3 GTPase cycle(HSA-9013423)
Organelle localization by membrane tethering(GO:0140056)
trans-Golgi network membrane(GO:0032588)
trans-Golgi network membrane(GOCC:0032588)
Phagocytic vesicle(GOCC:0045335)
trans-Golgi network(GOCC:0005802)
Phagocytic vesicle(GO:0045335)
Golgi apparatus subcompartment(GOCC:0098791)
trans-Golgi network(GO:0005802)
Endocytic vesicle membrane(GOCC:0030666)
Recycling endosome(GOCC:0055037)
Golgi organization(GO:0007030)
FDR
genes
GeneRatio

Figure 6

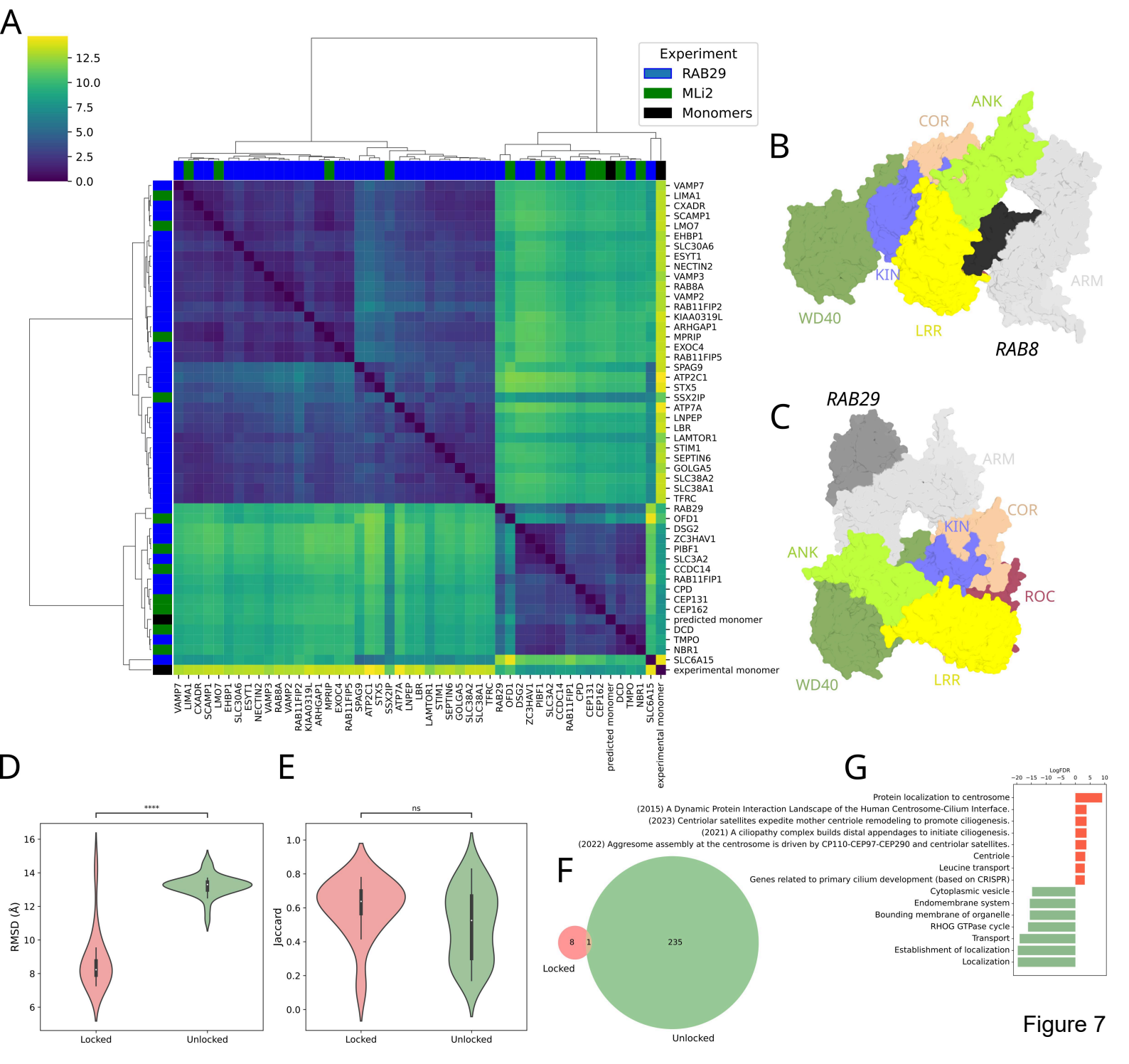
A
12.5
10.0
7.5
5.0
2.5
0.0
Experiment
RAB29
MLi2
Monomers
VAMP7
LIMA1
CXADR
SCAMP1
LMO7
EHBP1
SLC30A6
ESYT1
NECTIN2
VAMP3
RAB8A
VAMP2
RAB11FIP2
KIAA0319L
ARHGAP1
MPRIP
EXOC4
RAB11FIP5
SPAG9
ATP2C1
STX5
SSX2IP
ATP7A
LNPEP
LBR
LAMTOR1
STIM1
SEPTIN6
GOLGA5
SLC38A2
SLC38A1
TFRC
RAB29
OFD1
DSG2
ZC3HAV1
PIBF1
SLC3A2
CCDC14
RAB11FIP1
CPD
CEP131
CEP162
predicted monomer
DCD
TMPO
NBR1
SLC6A15
experimental monomer
B
ANK
COR
KIN
ARM
WD40
LRR
RAB8
C
RAB29
ARM
COR
KIN
ANK
ROC
WD40
LRR
D
****
RMSD (Å)
16
14
12
10
8
6
Locked
Unlocked
E
ns
Jaccard
1.0
0.8
0.6
0.4
0.2
0.0
Locked
Unlocked
F
8
1
235
Locked
Unlocked
G
LogFDR
−20 −15 −10 −5 0 5 10
Protein localization to centrosome
(2015) A Dynamic Protein Interaction Landscape of the Human Centrosome-Cilium Interface.
(2023) Centriolar satellites expedite mother centriole remodeling to promote ciliogenesis.
(2021) A ciliopathy complex builds distal appendages to initiate ciliogenesis.
(2022) Aggresome assembly at the centrosome is driven by CP110-CEP97-CEP290 and centriolar satellites.
Centriole
Leucine transport
Genes related to primary cilium development (based on CRISPR)
Cytoplasmic vesicle
Endomembrane system
Bounding membrane of organelle
RHOG GTPase cycle
Transport
Establishment of localization
Localization

Figure 7

A

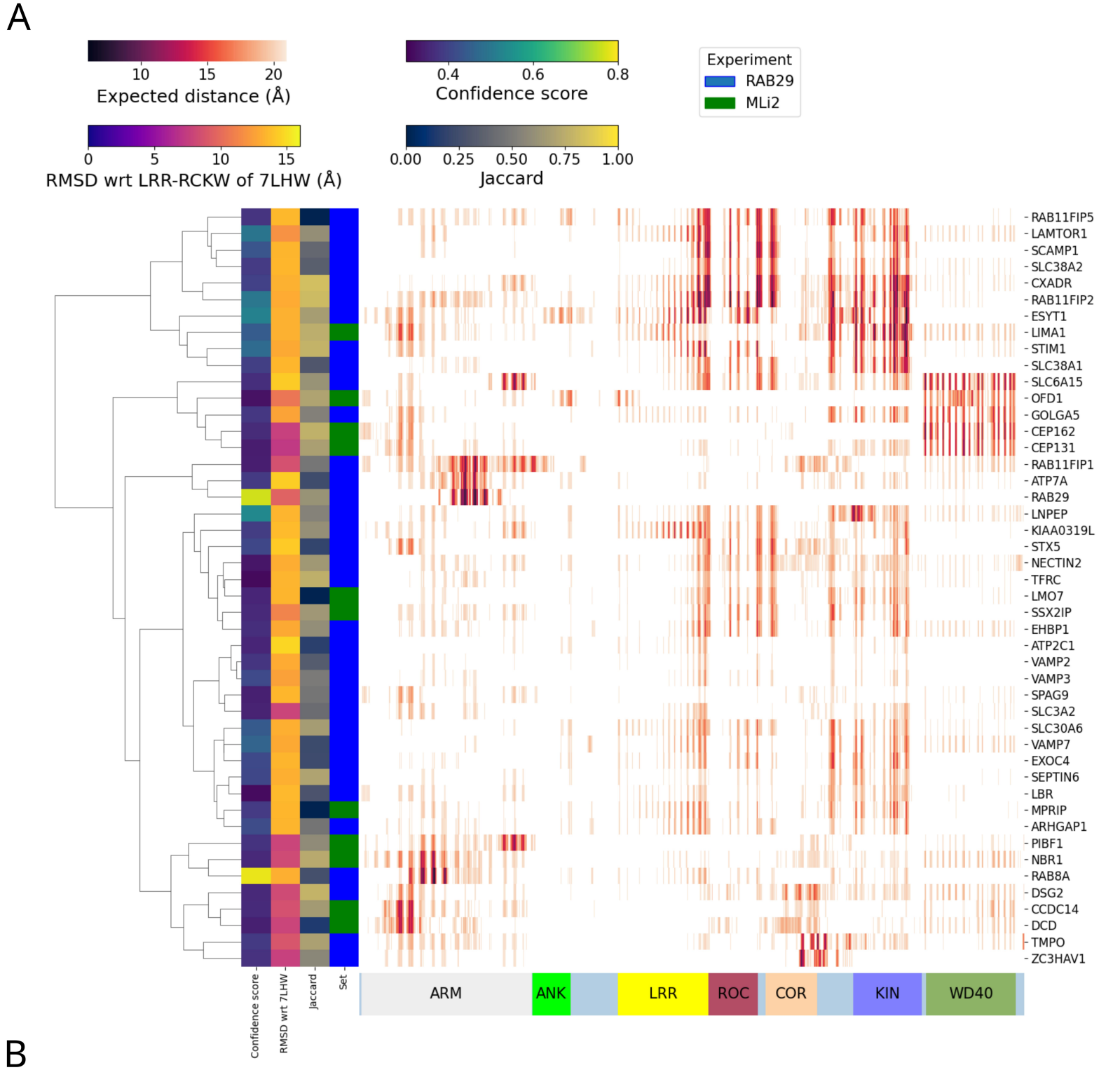

B

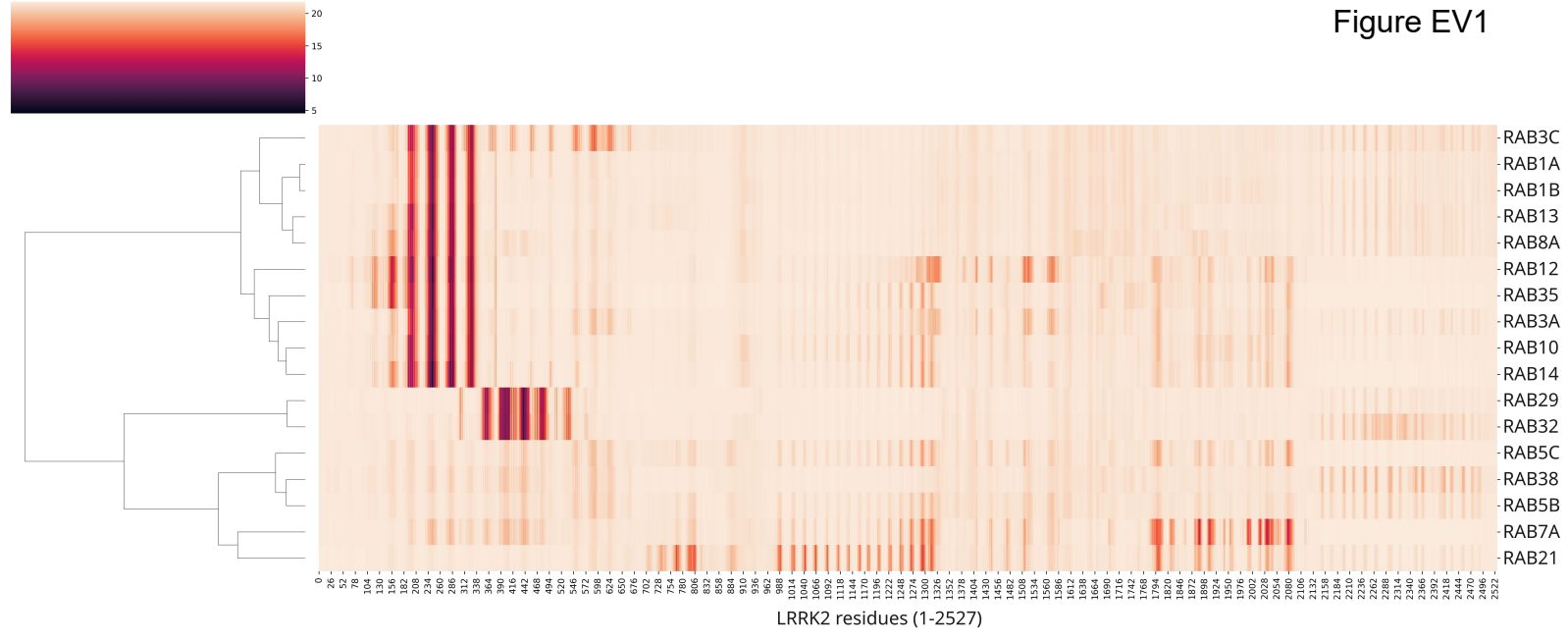

Figure EV1

Appendix

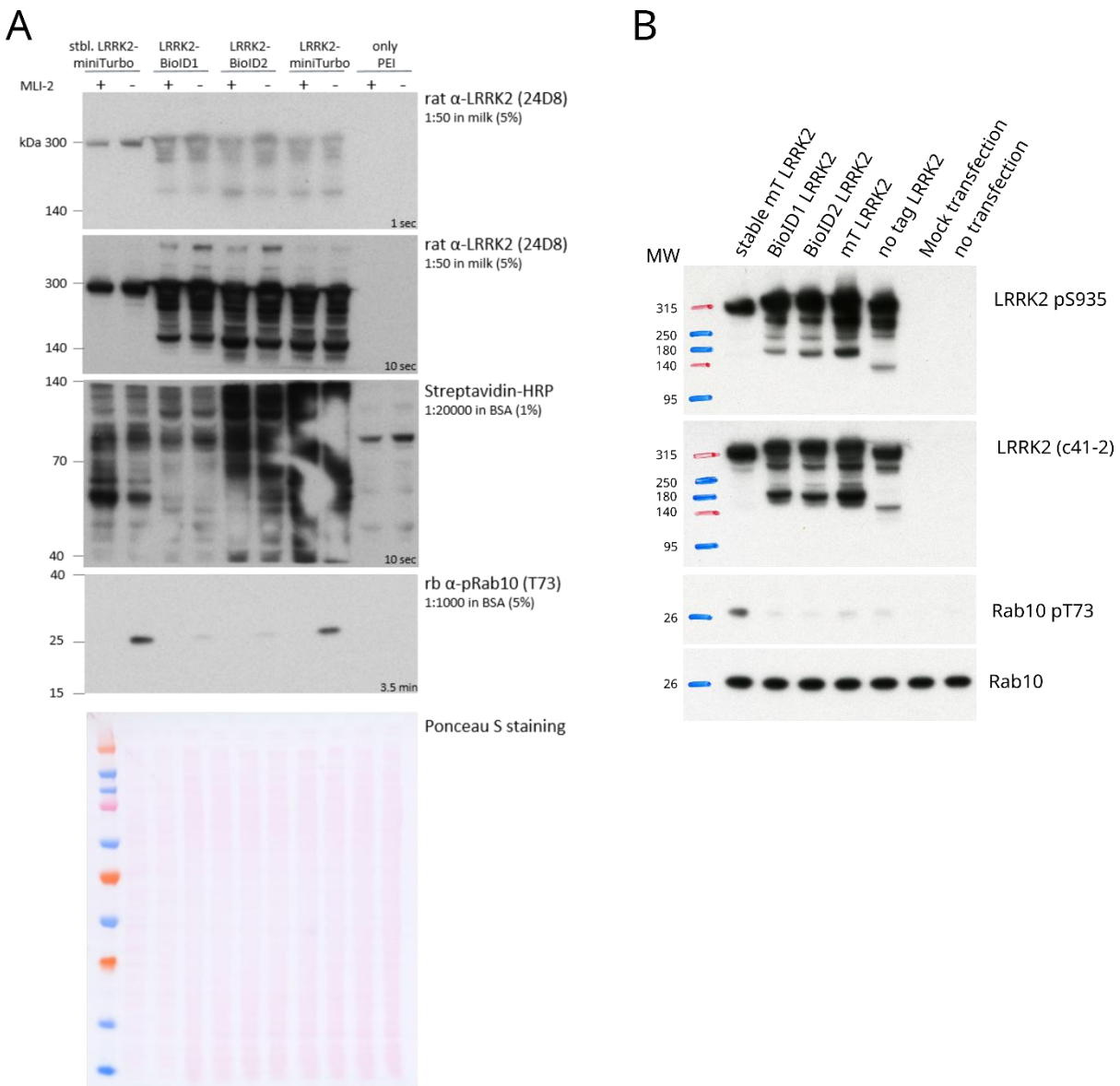

Appendix Figure S1: Western blot, pRab10, pS935 and biotinylation – comparison BioID1, BioID2, miniTurbo. To ensure functional BioID-fusion proteins, LRRK2 phosphorylation at S935 and Rab10 phosphorylation was assessed. (A) The different BioID LRRK2 constructs show sufficient biotinylation of proteins as well as MLi-2-responsive Rab10 phosphorylation. (B) All constructs are phosphorylated at S935 (top panel). Replication of LRRK2-mediated Rab10 phosphorylation (last panel) demonstrating functional BioID fusion proteins.

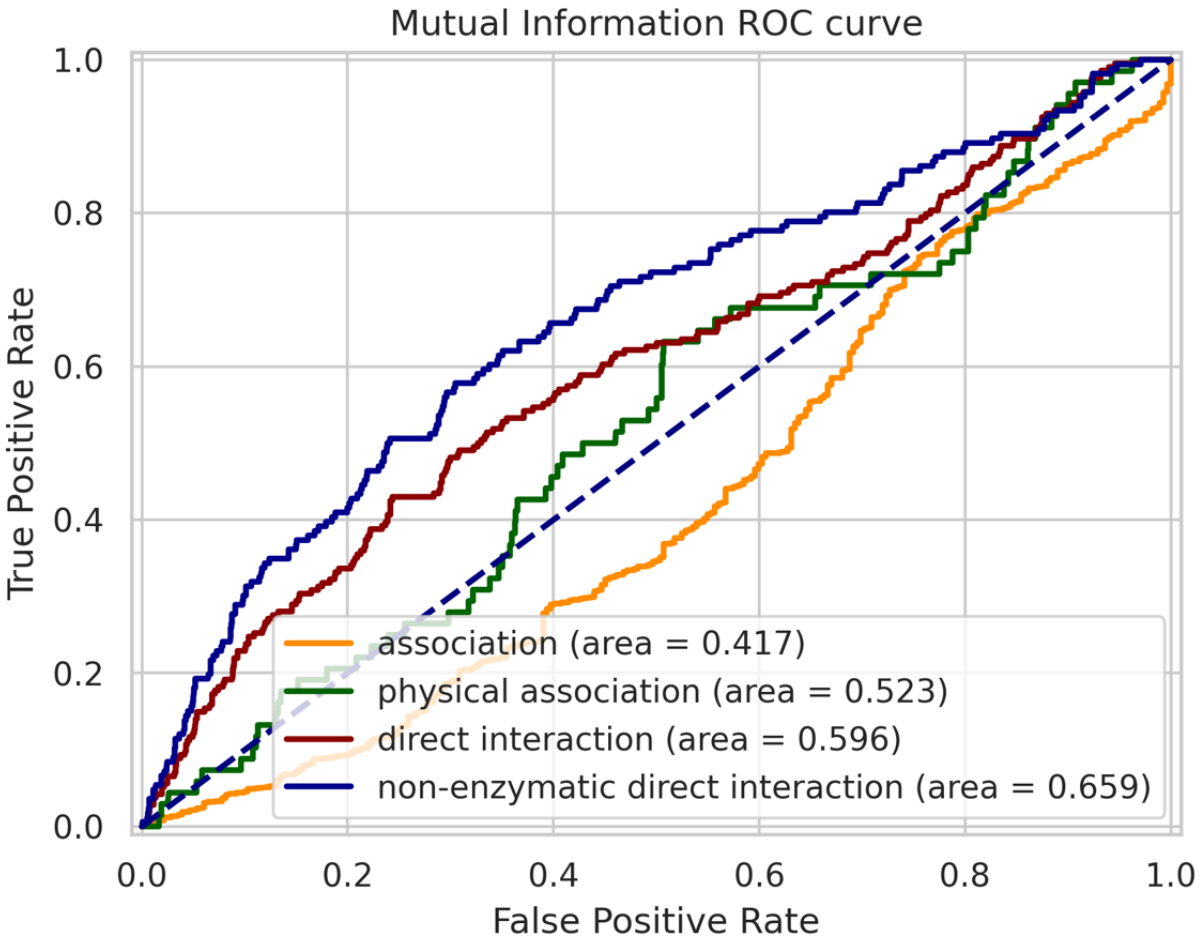

Appendix Figure S2: ROC Curve of prediction with Mutual Information (MI) of LRRK2's IntAct interaction types.

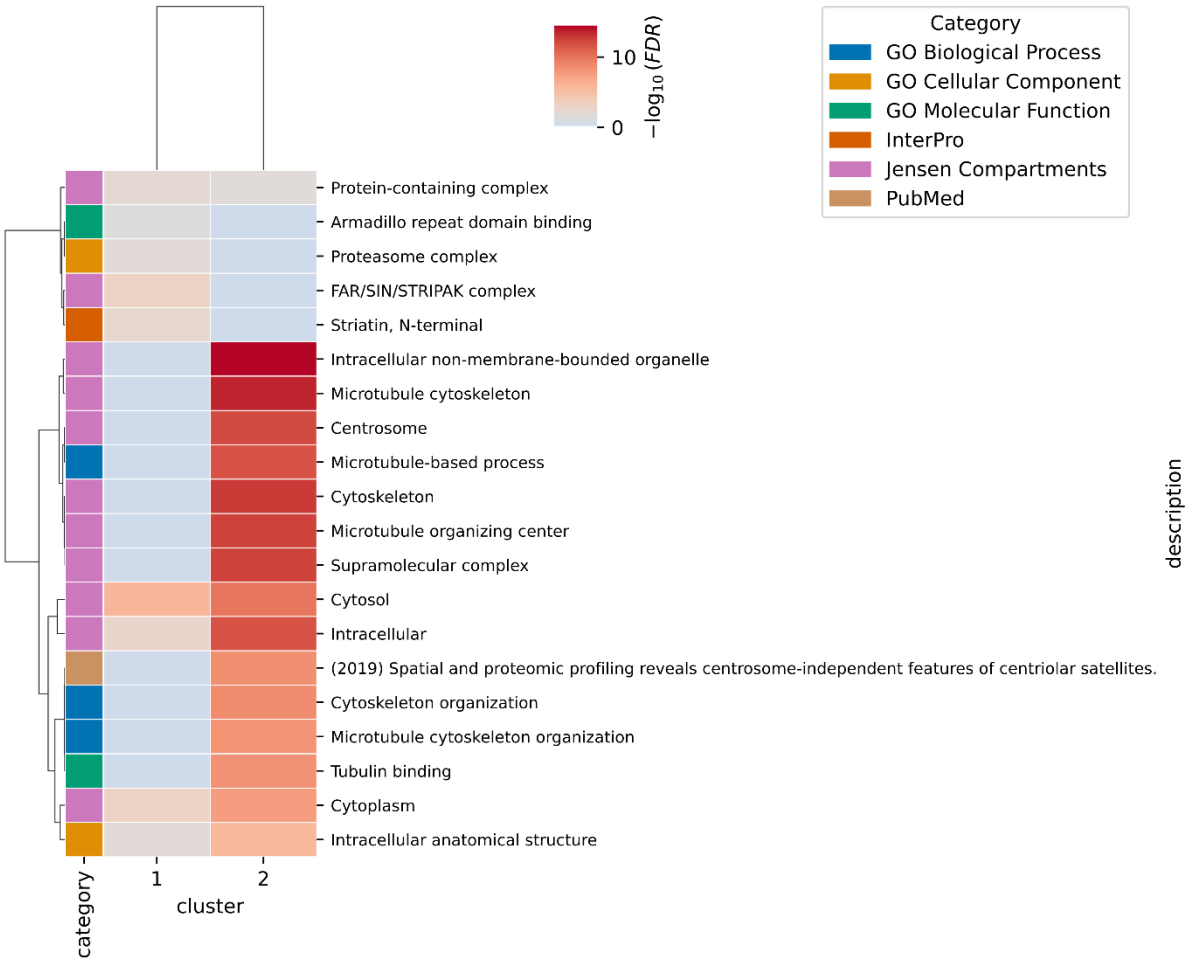

Appendix Figure S3: heatmap with cluster specific, significantly enriched processes (FDR < 0.01; StringDB) obtained from co-evolution (Jaccard)-based clustering of the LRRK2 BioID interactome.

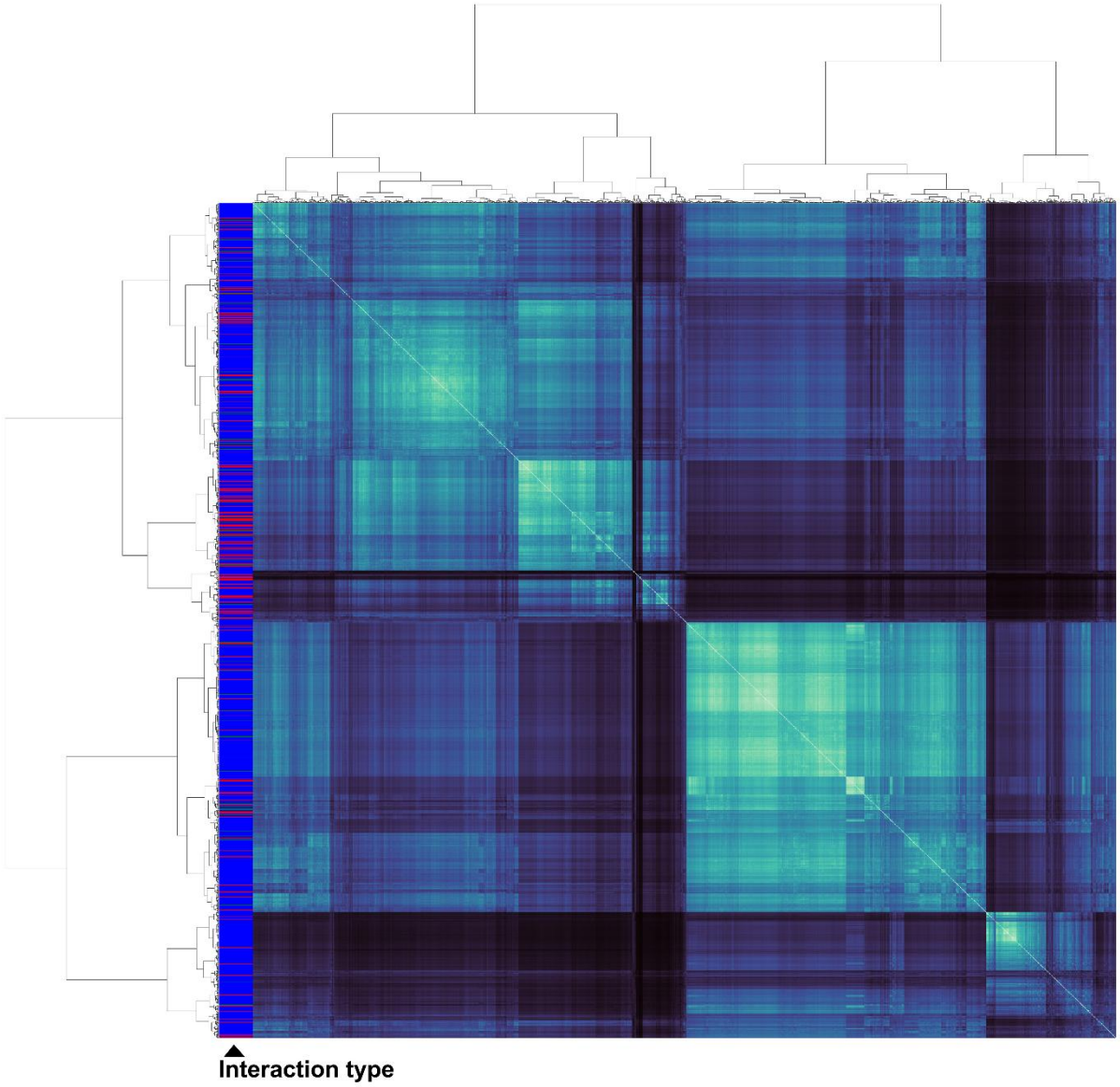

Appendix Figure S4: heatmap displaying the coevolution (Jaccard)-based hierarchical clustering of the LRRK2's IntAct interactome. Colored bars provide IntAct's interaction type annotation.

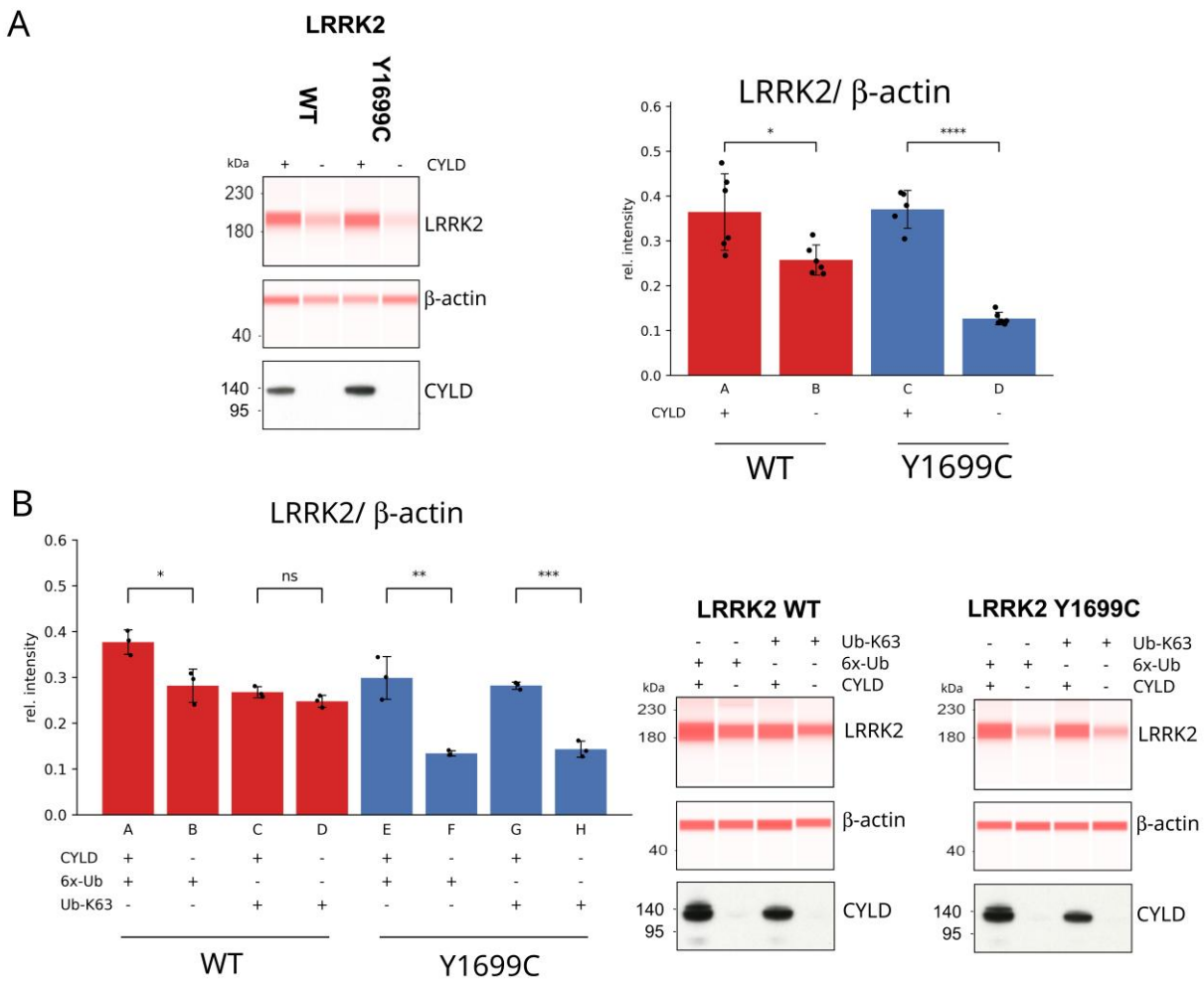

Appendix Figure S5: Effect of CYLD co-expression and ubiquitin derivatives on steady-state LRRK2 levels in WT and Y1699C variants (A) Effect of CYLD co-expression on steady-state LRRK2 levels (second independent experiment). LRRK2 WT or Y1699C was co-expressed with CYLD or empty vector control. LRRK2 protein levels were normalized by β-actin. Statistical significance was assessed using unpaired two-tailed t-tests (P-values: A-B: 0.0171; C-D: 3.0E-7; N = 6 biological replicates (for the Y1699C condition, one data point was skipped for technical reasons); error bars = SD) (left panel). Reconstructed Capillary Western signals and confirmation of CYLD expression by Western blot. On the capillary Western blot, LRRK2 migrates at a lower molecular weight (right panel). (B) Effect of ubiquitin conjugation type. LRRK2 WT or Y1699C was co-expressed with CYLD or empty vector control either in the presence of WT ubiquitin or K63-only ubiquitin (Lim *et al.*, 2005). Quantification of LRRK2 protein levels from three biological replicates. LRRK2 protein levels were normalized by β-actin. Statistical significance was assessed using unpaired two-tailed t-tests (P-values: A-B: 0.0218; C-D: 0.1289; E-F: 0.0037; G-H: 0.0002; N = 3 biological replicates; error bars = SD) (upper panel). Reconstructed Capillary Western signals and confirmation of CYLD expression by Western blot (lower panel).

A

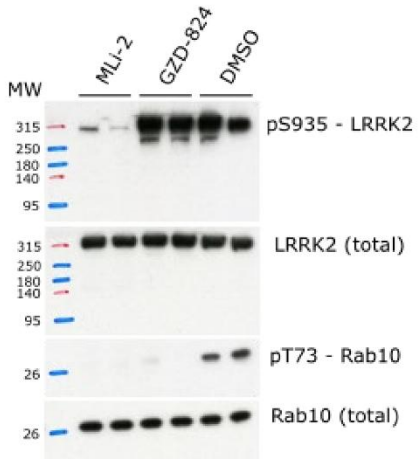

B

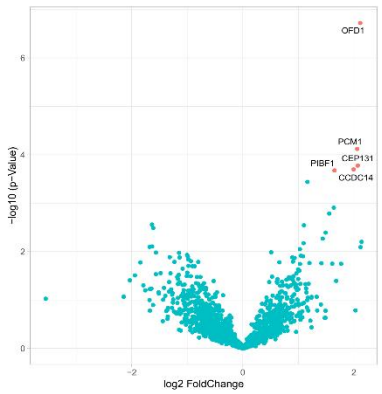

C

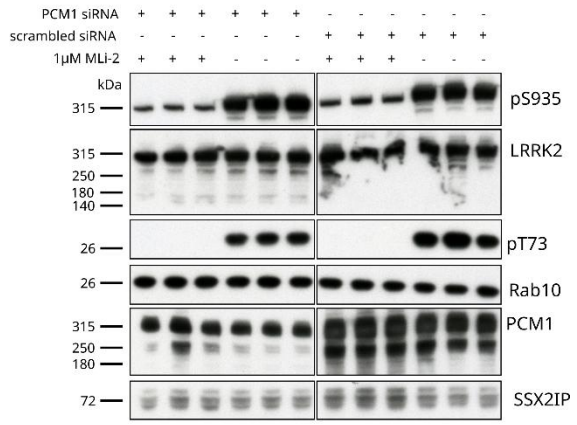

Appendix Figure S6: (A) Western blot analysis demonstrating effective LRRK2 inhibition by MLi-2 (type I inhibitor) and GZD-824 (type II inhibitor) in HEK293 cells stably expressing miniTurbo-tagged LRRK2. Both compounds at 1 µM significantly reduce Rab10 phosphorylation. As expected, MLi-2 induces a marked loss of LRRK2 pS935 phosphorylation, a hallmark of type I kinase inhibition. In contrast, GZD-824 does not affect pS935 phosphorylation, consistent with its classification as a type II inhibitor (Tasegian *et al.*, 2021). (B) BioID-based proximity labeling comparing the interactome changes upon treatment with MLi-2 versus GZD-824 (moderated permutation-based T-test, FDR = 0.05; S0 = 0.1; N = 7). Volcano plot illustrates differential protein interactions, highlighting the distinct molecular effects of type I and type II LRRK2 inhibition. (C) Validation of PCM1 knock-down by western blot. Efficient depletion of PCM1 is confirmed, with no observed changes in total protein levels of LRRK2, Rab10, or SSX2IP. LRRK2 inhibition by MLi-2 remains effective in the context of PCM1 knock-down.